

# Airfoil optimization using Design-by-Morphing

Haris Moazam Sheikh <sup>†</sup>, Sangjoon Lee <sup>†</sup>, Jinge Wang and Philip S. Marcus

Department of Mechanical Engineering, University of California, Berkeley, CA 94720, USA

\*Correspondence: [harissheikh@berkeley.edu](mailto:harissheikh@berkeley.edu)

†Equal contribution.

## Abstract

Design-by-Morphing (DbM) is a novel design methodology that creates a search space for topology optimization. Traditional design techniques often impose geometric constraints and, sometimes, the designer's biases on the design space, which restricts the novelty of the designs and allows for only small local changes. On the contrary, we show in this paper that DbM does not impose such restrictions on the design space, thus allowing for a radical and expansive search space with only a few design parameters. We compare DbM with other methods in the case of design space generation for 2D airfoils and find that DbM can reconstruct the entire UIUC database with >99.5% accuracy. Furthermore, using a bi-objective genetic algorithm, we optimize the airfoil designs created by DbM to maximize both the lift-over-drag ratio,  $CLD_{max}$ , and stall angle tolerance,  $\Delta\alpha$ , which results in a Pareto-front of innovative airfoils that exhibit substantial improvements in both objectives.

**Keywords:** design-by-morphing (DbM), topology optimization, airfoil

## 1. Introduction

Airfoil shape optimization is a critical stage in the design of aerodynamic components, such as aircraft wings (Drela 1998; Besnard et al., 1998; Vicini & Quagliarella 1999; Elham & van Tooren 2014) and wind-turbine blades (Li et al., 2010; Ju & Zhang 2012; Ribeiro et al., 2012; Grasso 2012; Chehouri et al., 2015; Ali & Kim 2021). The airfoil optimization process typically involves three main components: shape parametrization, airfoil evaluation, and optimization. Among these, the parametrization method defines both the design space and the complexity of the optimization problem. To ensure effectiveness, a desirable parametrization technique must be able to encompass a wide design space using a modest amount of design parameters (Sobester & Barrett 2008; Sripawadkul et al., 2010; Masters et al., 2015; Chen et al., 2017). This is particularly important during the initial design phase, where minimum geometric constraints are imposed, and the flexibility to make significant changes during optimization is beneficial.

Shape parametrization methods differ in their fidelity and control ranges (Masters et al., 2015; Sobester & Barrett 2008) and can be placed on a virtual spectrum according to the geometric scope of each design parameter. At one end of the spectrum, adjusting a single parameter alters a local section of the airfoil, which offers precise shape control but modifies the shape slowly. At the opposite end, each design parameter affects the global contour of the airfoil (Sobester & Barrett 2008).

At the local end of the spectrum is the discrete method (Jameson 1988), where the design parameters are exactly the discrete points that define the airfoil surface. Since the position of each point can be adjusted, the design space is potentially limitless (Samareh 2001) and precise local control with high fidelity can be achieved. However, a substantial number of surface points are needed to

accurately describe an airfoil shape, which complicates the optimization problem. Gradient-based optimizers are frequently employed to mitigate the increased complexity, but they are likely to get stuck at a sub-optimal solution during the optimization.

As the geometric scope of each parameter is expanded, there emerge the classical approaches that are based on the curve-fittings of regional features or control points. For example, the popular parametric section (PARSEC) method (Sobieczky 1999) uses 11 or 12 parameters to represent major sectional features of an airfoil, including leading edge radii and upper and lower crest locations, and constructs the airfoil surface using a sixth-order polynomial. Another popular method is the Bézier parametrization (Farin 1993), which constructs the upper and the lower surfaces of the airfoil through the Bézier curves defined by pre-chosen control points. Additionally, a hybrid of the two techniques, Bézier-PARSEC parametrization, was introduced by Rogalsky & Derksen (2009), which uses the parameters of the PARSEC method to define the Bézier curves that form the shape contours. One main issue with the above methods is their inability or inefficiency to include high-fidelity features; the PARSEC and the Bézier-PARSEC methods both have a fixed number of parameters and a limited range of fidelity, while the Bézier parametrization requires higher-degree Bézier curves to describe complex shapes which are inefficient to calculate (Samareh 2001).

To consider finer details of airfoils or, equivalently, to represent more complex curves, either B-splines (Sanaye & Hassanzadeh 2014; Han & Zingg 2014) or non-uniform rational B-spline (NURBS; Schramm et al., 1995) can be used, which creates curves by connecting low-order Bézier segments defined by control points. As the number of control points increases, these methods move to the local end of the spectrum and become capable of representing high-fidelity features, but the computing complexity also

Received: February 7, 2023. Revised: May 15, 2023. Accepted: May 18, 2023

© The Author(s) 2023. Published by Oxford University Press on behalf of the Society for Computational Design and Engineering. This is an Open Access article distributed under the terms of the Creative Commons Attribution-NonCommercial License (<https://creativecommons.org/licenses/by-nc/4.0/>), which permits non-commercial re-use, distribution, and reproduction in any medium, provided the original work is properly cited. For commercial re-use, please contact [journals.permissions@oup.com](mailto:journals.permissions@oup.com)

increases. One way to reduce the number of design parameters is to group the control points together so that global transformations such as twisting and thickening can be used as the parameters. This is known as the free-form deformation (FFD) method (Sederberg & Parry 1986; Lamousin & Waggenpack 1994) and is closer to the *global* end of the spectrum. A similar method, called the radial basis function (RBF) domain element approach (Buhmann 2003; Wendland 2005; Tang et al., 2020), also exists and makes use of RBF to exert deformation on the airfoil.

Near the *global* end of the spectrum, we see methods using spectral construction of basis functions to form or deform airfoil shapes. One popular choice of the basis functions is the dominant modes from singular value decomposition (SVD) of an airfoil dataset (Toal et al., 2010; Ghoman et al., 2012; Yonekura & Watanabe 2014; Kedward et al., 2020; Poole et al., 2019). Other choices include sinusoidal functions of the Hicks-Henne approach (Hicks & Henne 1978), which create 'bumps' on a reference airfoil surface, and surface functions of the class/shape function transformation method (Kulfan & Bussoletti, 2006; Akram & Kim, 2021), which are in the form of the product of a class function and a shape function generated by a linear combination of Bernstein polynomials. Nonetheless, like many other methods on the spectrum, these methods also suffer from the so-called *curse of dimensionality* that more basis functions or modes are always required to resemble high-fidelity features.

Efforts have been made to overcome the *curse of dimensionality* (Viswanath et al., 2011, 2014; Cinquegrana & Iuliano, 2018). A recent work by Chen et al., (2020) applied a generative adversarial network (GAN) to learn the major shape variations of an airfoil database and use those to parameterize the shapes while also preserving the high-fidelity features via an additional noise space. However, like many other dimension reduction methods, this study assumes that the optimum design is not far from the database, which is not always true. To address this limitation, they proposed another GAN-based method that encourages diversity during sample generation (Chen & Ahmed, 2020), but a large dataset is still required to initialize the training. In contrast, our paper is motivated by the optimization problem during the early design stage when few initial designs are available. Therefore, we are interested in a parametrization method that is capable of representing high-fidelity features even when the design parameters and initial airfoil designs are limited.

In this paper, we apply the Design-by-Morphing (DbM) parametrization technique to the airfoil optimization problem. DbM is a novel and universal design strategy that was first introduced by Oh et al., (2018) and has been used in recent years for geometry optimization of different problems (Oh et al., 2018; Sheikh & Marcus 2019; Sheikh et al., 2022, 2021). As a *global* method, it 'morphs' homeomorphic baseline shapes together to create new shapes and is able to interpolate and extrapolate the design space, allowing for both high-fidelity representation of shapes without the curse of dimensionality and radical modifications to the shapes without any implicit geometric constraints (Oh et al., 2018; Sheikh et al., 2022). This strategy is applicable to a variety of 2D and 3D design problems, and we aim to conduct a special case study of DbM for the 2D airfoil shape optimization here. Throughout this paper, we aim to make the following scientific contributions:

- Application of DbM to 2D airfoil shape optimization, showing its accurate reconstruction of the existing airfoil database and radical changes in airfoil shapes while being free from ge-

ometric constraints and designers' biases by extrapolation of the design space by applying negative weights.

- Evaluation of airfoil design capacity of the DbM strategy and comparison with other typical 2D airfoil design strategies.
- Sensitivity analysis for the number of baseline shapes convergence analysis compared to conventional airfoil design strategies is shown, and the significance of extrapolation for DbM is also shown.
- Optimization within the 2D airfoil search space generated by DbM using a genetic algorithm (GA) and investigation of the optimum Pareto-front.

## 2. Design-by-Morphing

Design-by-Morphing (DbM) works by morphing homeomorphic, i.e., topologically equivalent, shapes to create a continuous and constraint-free design search space. It comes with several advantages. To begin with, DbM is valid for shapes of any dimension and capable of creating exotic shapes because radically different baseline shapes can be morphed together. Furthermore, DbM does not impose any geometric constraints on the design parameters. And the only implicit constraints are the selections of the 'baseline shapes' themselves, which are necessary to prescribe the problem to be solved. Lastly, it is able to create an extensive design search space, even when the number of pre-existing designs is small, e.g., (Sheikh et al., 2022), by both the means of 'extrapolation,' that is to assign negative weights during morphing, and the inclusion of irregular or uncommon shapes. The details of DbM for airfoil optimization are presented in the subsequent subsections.

### 2.1 Baseline shapes and morphing

The DbM technique requires two or more homeomorphic 'baseline shapes,' mostly chosen from pre-existing designs in the literature, to create the design space. A one-to-one correspondence between the baseline shapes must first be established through some systematic shape collocation methods in either the functional (Oh et al., 2018) or the geometric space (Sheikh & Marcus, 2019; Sheikh et al., 2022). Then the new shapes can be generated by applying weights to the collocation vectors of the baseline shapes and summing them together in a linear manner.

For 2D airfoils, the closed shapes can be collocated in the Euclidean coordinate system. It is noted here that all 2D shapes bounded by a single surface are homeomorphic to one another. Using the leading edge of each airfoil as origin, each shape can be collocated by taking fixed and uniformly spaced points along the x-axis, creating a one-to-one correspondence between the shapes. This collocation strategy is demonstrated in Fig. 1, and the baseline shapes used in this paper are chosen from various airfoils in the literature, which are detailed later. Morphing is performed by multiplying a specific airfoil shape with a scalar weight, summing the weighted vectors, and then normalizing them. For a collection of  $N$  baseline shapes, morphing is given by

$$\mathbf{P}(\mathbf{x}) = \frac{1}{\sum_{m=1}^N w_m} \sum_{n=1}^N w_n \mathbf{S}_n(\mathbf{x}). \quad (1)$$

Here,  $\mathbf{S}_n(\mathbf{x})$  is the y-coordinate collocation vector of the  $n^{\text{th}}$  baseline shape, collocated at  $\mathbf{x} = [x_0, \dots, x_F]$  where the  $i^{\text{th}}$  x-coordinate  $x_i = |1 - 2i/F|$  and  $F$  is the number of collocation points. The first half of the elements of  $\mathbf{S}_n$  represents the top surface of the airfoil, and the second half of the elements of  $\mathbf{S}_n$  represents the bottom.  $w_n \in [-1, 1]$  is the morphing weight applied to the y-coordinate vector of the  $n^{\text{th}}$  baseline shape, and negative  $w_n$  values imply

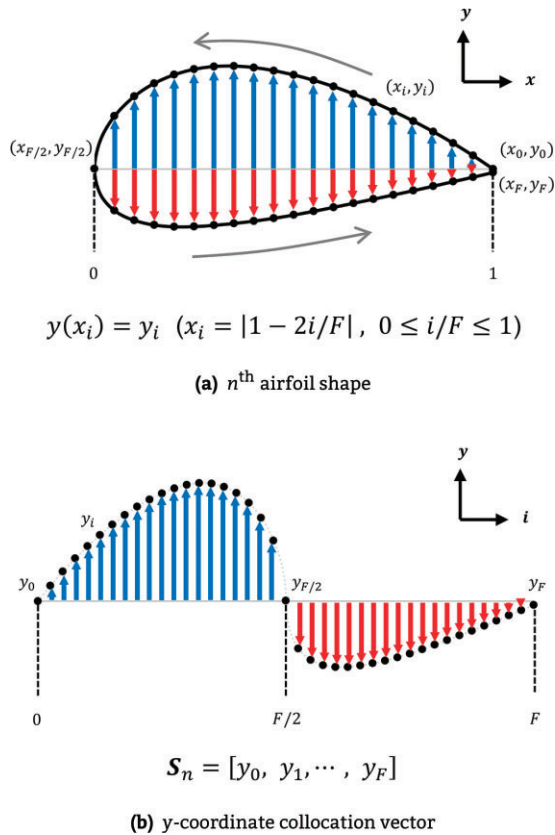


**Figure 1:** An example of DbM. The coordinates of the baseline shapes are weighted, summed, and normalized to form the coordinates of a morphed shape.

extrapolation. A visual demonstration of the strategy is presented in Fig. 2.

## 2.2 Intersection control

For smooth baseline shapes, applying positive weights, i.e., interpolation, will always create smooth shapes. However, applying negative weights, i.e., extrapolation, may produce non-physical geometries, such as self-intersections, which have ‘zero-area’ regions, as shown in Fig. 3a. One may discard the morphed airfoil shapes with self-intersections during the optimization, but that diminishes the size of our design space. Instead, we recover new shapes by removing the intersections.

Intersection removal is accomplished by first locating the intersection within the morphed coordinate vector and restructuring the vector by ‘flipping’ it between the intersection points, as shown in Fig. 3c. The vector is then ‘stiffened’ to remove the ‘zero-area’ between the intersections by removing the points in their neighborhoods and linearly interpolating between the broken coordinate vectors. As seen in Fig. 3d, this removes the ‘zero-area’ space and adds some physical area to the shape at the original intersection point. This process is repeated until all intersections are removed, e.g., both intersections in Fig. 3 are successfully removed, and finally, a moving-average smoothing filter is applied to smooth out any sharp edges.

## 2.3 Selection of baseline shapes

The selection of baseline shapes is a crucial component of the DbM strategy and ultimately determines the size and novelty of our search space. Metaphorically, the selection of the baseline air-

foil shapes serves as the gene pool for the morphed airfoils and its diversity is important for creating a large design space.

One way of selecting the baseline shapes is by performing SVD or principle component analysis (PCA) on a set of shapes and then using the dominant modes as the baseline shapes. Methods such as parametric model embedding Serani & Diez (2023) can help reduce the dimensionality of the problem as well. Although these methods would help in quantitatively choosing baselines, these methods, however, require an existing dataset that might not be available in many shape optimization problems (Oh et al., 2018; Sheikh et al., 2017, 2022). Therefore, while techniques like SVD and PCA can be easily applied to airfoil shape optimization problems and provide arguably better baselines, we choose the baseline shapes qualitatively instead to demonstrate the universality of DbM even for engineering problems with few existing designs. In other words, for research purposes, we assume that the airfoil database is not *a priori* knowledge at the selection stage, except for those chosen as baselines.

An additional benefit of directly morphing existing designs is that, from a human designer’s perspective, it can be more intuitively informative than handling PCA modes. For example, vertical-axis wind turbines are broadly categorized into drag, lift, and hybrid categories, so the weights associated with each type are more informative to a human designer than the weights of the dominant modes. On the other hand, choosing actual shapes as the baseline shapes has the advantage that non-conforming designs can be easily added, as is the case for baseline #19 (mirrored Selig airfoil). Conventional techniques may have much more difficulty adding radical features into the design space, and the significance of such radical baseline shapes is demonstrated in the Results section.

We selected 25 shapes (see Fig. 4) from the UIUC airfoil coordinates database (Selig, 2022) as our baseline shapes. They were picked to ensure diversity and to introduce radical features into the design space. Our selection of baseline shapes included airfoils that are either known for high lift-to-drag ratio or good stall performance, which are commonly used in the literature and the industry. We also included airfoils with poor aerodynamic performances, as well as airfoils with irregular shapes, to provide novelty to the design space. It is worth noting that, unlike in the conventional airfoil optimization processes (Koroglu & Ozkol, 2019), we deliberately included the bad performers so that our optimization could suppress these features by assigning them negative weights, which will be demonstrated in greater detail in our later results. The model names and characteristics of the baseline shapes can be found in Appendix B. To express shapes as collocation vectors, each airfoil shape is represented by 4001 coordinates that span counterclockwise from the upper surface trailing edge around the leading edge to the lower surface trailing edge, with equally distributed  $x$ -coordinates parallel to the airfoil chord line of unit length (i.e.,  $F = 4000$  in Fig. 1).

## 2.4 Airfoil design capacity test

As a benchmark, we reconstruct the entire UIUC airfoil database (Selig, 2022) using DbM to test the robustness of our method and the representation capacity of the generated design space. Having noted that one of the key features of DbM is to permit shape extrapolation, we compare our reconstruction results against the results of an interpolation-only DbM (DbM-I) where all DbM weights are non-negative. In addition, we performed the same test on three conventional 2D airfoil shape parametrization methods: PARSEC (Sobieczky, 1999), NURBS (Schramm et al., 1995), and the

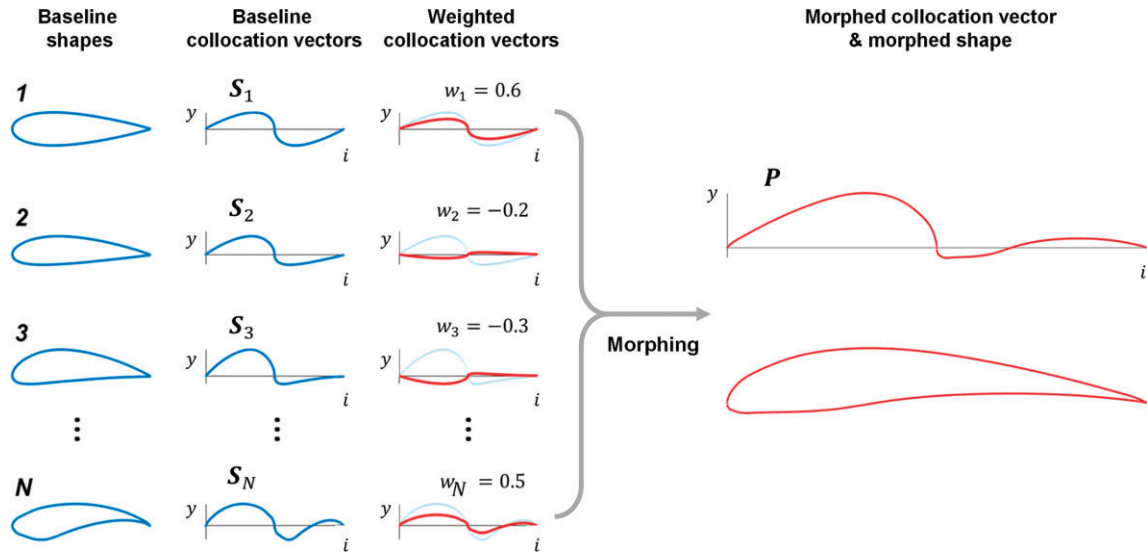


**Figure 2:** Application of DbM to 2D airfoils. Column 1 shows the baseline shapes. Column 2 depicts the elements of the collocation vectors of the baseline shapes plotted as a function of the index  $i$  of the collocation vector. Column 3 shows the weighted elements of the collocation vector plotted as a function of the index  $i$  of the collocation vector. Column 4 shows the resultant collocation vector of the morphed shape and the morphed shape itself.

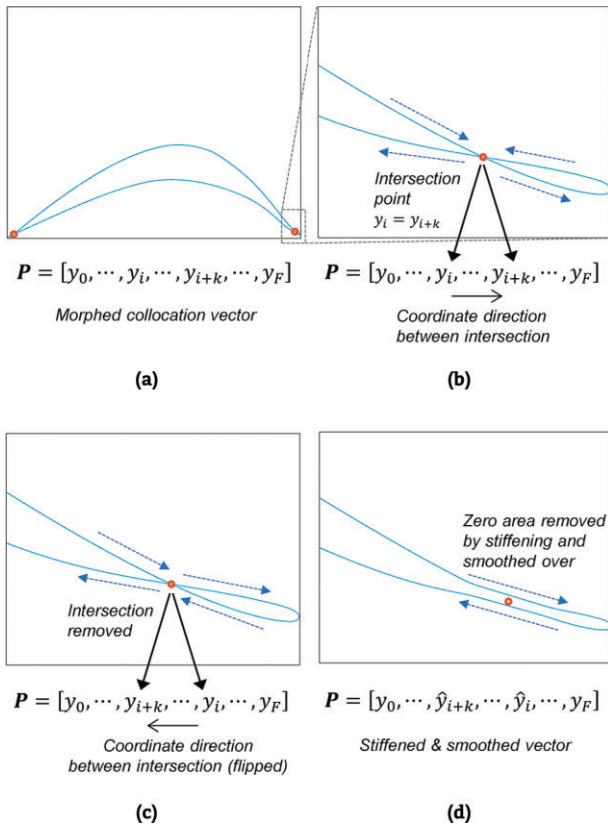


**Figure 3:** Conditioning for intersection removal. (a) Intersections are detected; (b) A blown-up image of one intersection, with the shape coordinates direction depicted by arrows; (c) Intersection removed by flipping the vector between the intersection; (d) The 'zero-area' removed by linear interpolation and then smoothed over, as shown by hatted  $y$ -coordinates.

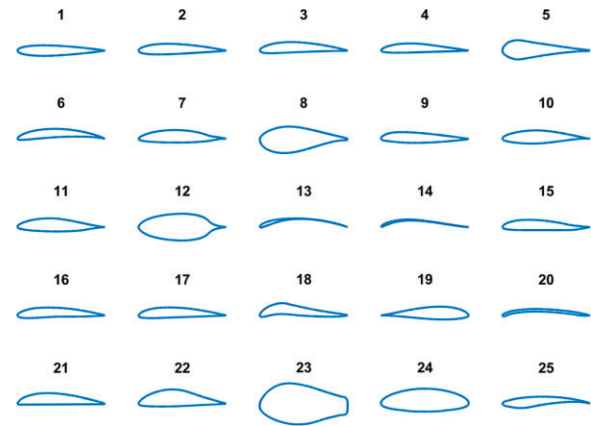


**Figure 4:** Twenty-five baseline airfoil shapes chosen from the UIUC database (Selig, 2022). See Appendix B for further details.

Hicks-Henne approach (Hicks & Henne, 1978). These tests were meant to answer the following questions:

- How much does the extrapolation expand the design space?

Extrapolation is undoubtedly better at creating a wider design search space. However, we shall focus on how *quantitatively* the search space is broadened by extrapolation, so as to confirm whether this feature genuinely distinguishes DbM from other generic approaches.

- Is DbM comparable to conventional airfoil shape parametrization methods in terms of shape reconstruction?

It should be noted that we selected the baseline airfoil shapes for DbM solely based on the qualitative principle of ensuring diversity and intentionally avoided the use of a selection method that requires a known, rich design database in advance. We shall demonstrate that the answer to the above question is still positive,



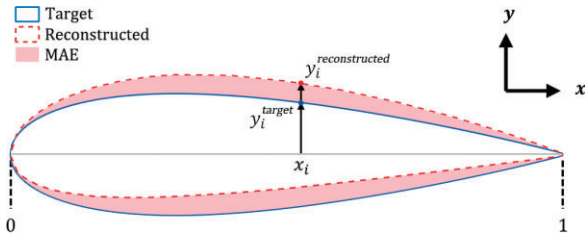


**Figure 5:** Geometric demonstration of MAE between target and reconstructed airfoil surfaces.

even though DbM is not a design method specifically for airfoils, unlike the methods that the DbM is compared with.

For all of the 1620 airfoils in the UIUC database (Selig, 2022), we obtained the closest representation of each target shape by running a global optimization of the input design parameters that minimizes mean absolute error (MAE) between the target and the reconstructed airfoil surfaces. A geometric demonstration of MAE is provided in Fig. 5. Using the functional expression of an airfoil  $y(x_i) = y_i$  ( $0 \leq i \leq F$ ), as introduced in Fig. 1a,

$$\text{MAE}(\text{target}, \text{reconstructed}) = \frac{2}{F} \int_0^F y_i^{\text{error}} di, \quad (2)$$

where  $y_i^{\text{error}} \equiv |y_i^{\text{reconstructed}} - y_i^{\text{target}}|$ . When we express the error in percentage terms, i.e.,  $(\text{MAE} \times 100)\%$ , we emphasize that the error is described as a proportion of the area difference to the square of the chord length, as all airfoil shapes are normalized to maintain a unit chord length. The factor of 2 in equation (2) is present for this reason.

To obtain the closest representation, we utilized a MATLAB-based single-objective GA: *ga*. The population size is set to 100, and the maximum number of generations is set to 500. The lower bound for MAE was set to  $1.44 \times 10^{-3}$  (or 0.144%) from equation (2) for a chord length of 1, in accordance with the lower limit of Kulfan's typical wind-tunnel tolerance (Kulfan & Bussoletti, 2006; Masters et al., 2017). To ensure a fair comparison, all the airfoil parametrization methods tested underwent the same optimization scheme for shape reconstruction, with similar numbers of design parameters (e.g., 25 design parameters for the DbM) except for PARSEC, which has fixed design parameters. In general, the fidelity of these design methods improves as the number of design variables increases (Masters et al., 2017).

It is important to note that the objective of our reconstruction tests is to examine both the efficiency and the accuracy of a given parametrization method in the context of shape generation during the design process, which must be distinguished from the accuracy in surface fitting. NURBS, for instance, can achieve arbitrary accuracy for shape fitting if a good initial guess of the parameters is provided, but it may not be ideal for shape generation as the shape it constructs varies slowly during the optimization process. Accordingly, all the reconstruction tests are initialized in a consistent manner to provide a meaningful comparison. In particular, the initial population is set to contain a single parameter set that represents the profile of NACA 0012 with the remaining sets randomly distributed. The results of the reconstruction tests can then be understood as the ability of a method to create various shapes, including the common designs that have been collected in the UIUC database, precisely within a certain number of optimization generations. And the progressive improvement in the design space reconstruction can be observed as a function of the number of GA generations.

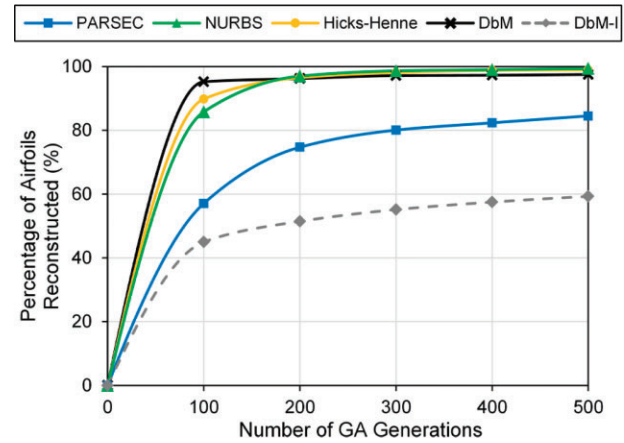


**Figure 6:** Percentage of airfoils reconstructed within the MAE tolerance of 0.5% using DbM, compared to those from DbM only with interpolation (DbM-I) and three airfoil shape parametrization methods (see Table 1).

Applying DbM for the reconstruction of the UIUC database, we found that 1618 of the 1620 airfoils of the entire UIUC database, were reconstructed with an MAE error  $< 1\%$ . Even for the two airfoils with the highest error, the DbM reconstruction still resulted in an MAE error of less than 1.5%. Figure 6 displays the percentage of airfoils that were reconstructed within the tolerance of 0.5% MAE error, with respect to the total number of GA generations. A comparison between DbM and DbM-I reveals that the extrapolation feature of DbM significantly contributes to the improved performance of the method, suggesting that the extrapolation feature is indispensable for DbM. On the other hand, at the maximum GA generation, the total percentage of reconstructed airfoils with an MAE error  $< 0.5\%$  increases from 60% (DbM-I) to 98% (DbM). As a result, DbM converges faster than any other conventional approaches tested here.

To provide better insight, we plot the reconstruction results of 10 airfoil shapes in Fig. 7, which represent the less successful reconstruction attempts. In particular, we ranked the results based on the unweighted average of all MAE errors from the five tested methods for each airfoil case and made the selections at every percentile bin from the worst. These 10 shapes are depicted in row-major order, from one in the 90<sup>th</sup> percentile (HOR 20, average MAE 0.35%) to one in the 99<sup>th</sup> percentile (FX 79-W-660A, average MAE 1.1%). Even these less successful results appear to reasonably reconstruct the target airfoil shapes. It is worth paying attention to the worst case, FX 79-W-660A, which is designed for use on a thick rotor blade of a wind turbine and far from the typical streamlined airfoil shapes. DbM-I encountered a notable failure in this case because none of our chosen baseline airfoil shapes for DbM were as thick as the target shape. As a result, the reconstruction just ended up with the thickest baseline airfoil shape, #23 (see Fig. 7e). This specific example underscores the significance of the extrapolation feature of DbM, which provides the opportunity to explore extraordinary designs, such as much thicker airfoils in this case. We also observed that NURBS occasionally produced thorn-like local structures (e.g., at the leading edge of GOE 511 in Fig. 7b), which resulted from the locally deforming nature of NURBS. These artifacts are normally removed by fitting software, such as FitCrv in Rhinoceros 3D, or by manual handling of the control points by the designer.

Another way DbM explicitly introduces novelty is by using novel shapes directly as baselines. Generally speaking, novel designs that contain unconventional features can be challenging to

**Table 1:** Airfoil shape parametrization methods for comparison.

Method	Design variables (DVs)	# of DVs	Remark
PARSEC	$r_{le}^{up/lo}$ : Leading edge radii $x_{up/lo}^{up/lo}, y_{up/lo}^{up/lo}$ : Crest coordinates $y_{xx}^{up/lo}$ : Crest curvatures $y_{te}, t_{te}$ : Trailing edge mid-position and thickness $\alpha_{te}, \beta_{te}$ : Trailing edge direction and wedge	12	Fixed # of parameters
NURBS	$x_{ctrl,i}^{up/lo}, y_{ctrl,i}^{up/lo}$ : Control point coordinates ( $i = 1, \dots, 4$ ) $w_i^{up/lo}$ : Curve weights ( $i = 1, \dots, 4$ ) $y_{te}^{up/lo}$ : Trailing edge positions	26	Third-order B-spline Evenly distributed knots
Hicks-Henne	$w_i^{up/lo}$ : Bump widths ( $i = 1, \dots, 6$ ) $m_i^{up/lo}$ : Bump magnitudes ( $i = 1, \dots, 6$ )	24	Base profile: NACA 0012 Cosine-distributed bump points
DbM (Present)	$w_i$ : Morphing weights ( $i = 1, \dots, 25$ )	25	See Fig. 4 for the baselines

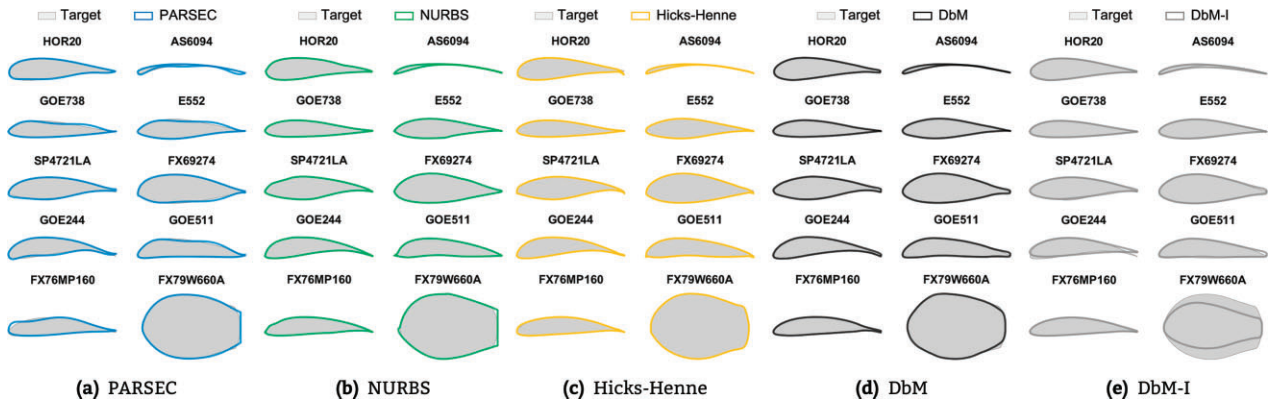


**Figure 7:** GA-based reconstruction of pre-existing airfoil shapes using different design parametrization methods, after 500 GA generations in total.

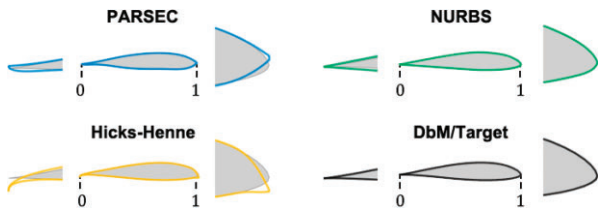


**Figure 8:** Reconstruction of a deliberately “mirrored” airfoil shape. In contrast to convention, the blunt edge is at  $x = 1$  and the sharp edge is at  $x = 0$ . PARSEC and the Hicks–Henne method, which implicitly define edge geometries, face challenges in reconstructing the mirrored edges. NURBS looks to perform well due to its better flexibility in adjusting curvatures through weights. DbM has no problem because it can take such non-conforming shapes as baselines as needed.

construct. For example, the ‘mirrored’ airfoil in our DbM baseline shapes (#19) is considered off-design by conventional airfoil parametrization methods that prescribe fixed edge geometries for the airfoil, such as relatively ‘blunt’ and ‘sharp’ edges at  $x = 0$  and  $x = 1$ , respectively. Figure 8 displays the results of the GA-based reconstruction of the mirrored airfoil using the tested methods. PARSEC and the Hicks–Henne approach, which implicitly define edge geometries for airfoils, clearly struggle in reconstructing the mirrored edges. At  $x = 1$ , these methods still exhibit hints of the sharp edge in their reconstructed shapes. On the other hand, NURBS performs well as it is more flexible in handling curvatures through weight parameters. However, although not considered in this study, if one wishes to introduce a tentative higher-order feature, such as a stepped wing (Lumsdaine *et al.*, 1974), NURBS may require a larger number of design parameters (i.e., more control

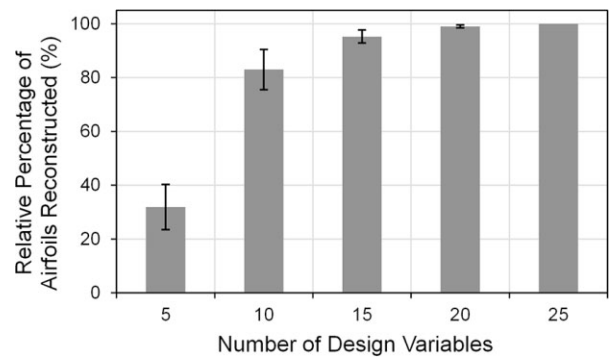


**Figure 9:** Relative percentage of airfoils reconstructed within the MAE tolerance of 0.5% by DbM using a subset of the chosen baseline shapes (see Fig. 4) to those using all 25 baseline shapes at the maximum GA generation. All tests were done five times with five random subsets for each case. Error bars indicate the standard deviation of the five test results.

points and weights). On the contrary, DbM would only require one additional design parameter (i.e., by adding it as a new baseline shape) to introduce novelty regardless of the complexity of the new design.

For the current study, we note here that we used 25 baselines based on the computational budget available, and our study shows that the number of baseline shapes was sufficient. However, a smaller number of baseline shapes might have proven to be enough as well to this end. Fig. 9 presents a sensitivity study of DbM in relation to the number of design variables (baseline shapes) used, where the convergence trend confirms that 20–25

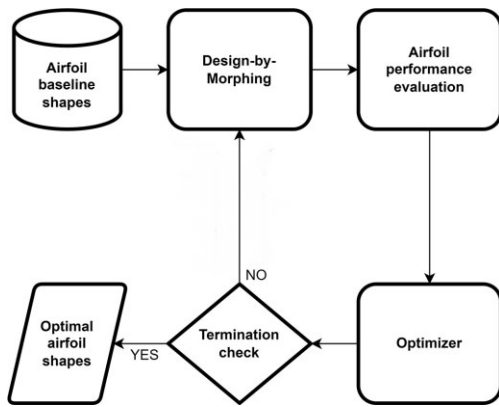


**Figure 10:** General flowchart of airfoil optimization via DbM.

baseline shapes are sufficient. Note that the current sensitivity study is restricted to the same baseline shape set in Fig. 4. All tests were done five times with five random subsets for each case to consider sensitivity to the choice of baseline shapes within the subset. Future efforts will be directed toward conducting additional sensitivity analyses of DbM by varying the selection of the initial 25 baseline shapes themselves.

Overall, we have shown that DbM is competitive against conventional local parametrization methods despite being on the global end of the spectrum. In addition, DbM's ability to generate extraordinary designs through the extrapolation feature enhances the chances of finding novel solutions that deviate from the inputs (baseline shapes), which is important because the aerodynamic performance of an airfoil can be non-intuitively correlated with geometric features of the airfoil. More importantly, DbM is not just a method for design parametrization, but rather, a universal design strategy for broader design search. While we have compared DbM to airfoil shape parametrization methods in the context of airfoil optimization, DbM can be useful for any type of problem that aims to introduce more novelty in design search.

### 3. Optimization Methodology

Our airfoil optimization methodology is built around the DbM technique introduced in Section 2. As shown by the flowchart in Fig. 10, the optimization starts with the selection of the baseline shapes and then evaluates and optimizes the airfoils formed by morphing these baseline shapes using DbM. Our methodology does not rely on a specific airfoil evaluation tool or a specific optimizer, and discussions on their choices are provided in Sections 3.1 and 3.2, respectively.

#### 3.1 Airfoil evaluation

Our optimization methodology is not limited to a specific airfoil performance analyzer. Any reliable CFD or experimental methods can be used. For optimizing airfoil shapes using CFD-based solvers, the evaluation of the objective functions (i.e., aerodynamic properties) is typically divided into two categories: the full Reynolds-averaged Navier-Stokes (RANS) based approach and the interacted viscous/inviscid zonal approach. The RANS-based approach is computationally expensive and demands a highly efficient optimizer. To accommodate a large number of design variables, which is common in aerodynamic designs, a gradient-based optimizer coupled with adjoint methods for computing derivatives is deemed most feasible (Kenway & Martins 2016;

He et al., 2019; Piotrowski & Zingg 2022). On the other hand, the viscous/inviscid zonal approach, which combines separated solutions for inviscid external flow and viscous shear layer flow in an iterative manner to form a continuous profile, is faster and less expensive.

Among a number of inviscid/viscous zonal airfoil analysis codes, XFOIL (Drela 1989) has been the most dominant and widely adopted program (Ronsten 1992; Giguère & Selig 1998; Jones et al., 2000; Mueller & DeLaurier 2003; Johnson et al., 2005; Batten et al., 2006; Lafountain et al., 2010; Ramanujam & Ozdemir 2017; Chen & Ahmed 2020). It combines a vorticity panel method for exterior flow with an integral boundary-layer method for viscous boundary layers and uses an  $e^9$ -type amplification formulation to determine the transition point (Drela 1989). Its suitability for airfoil designs has been demonstrated in the past literature, where its predictions of aerodynamic properties are found to be in good agreement with both wind-tunnel experiment data (McGhee et al., 1988; Selig et al., 1995) and the RANS-based simulation results (Morgado et al., 2016).

While our choice of the evaluation tool is flexible, for this work, we opt for XFOIL due to its acceptable accuracy under our flow condition and its low computation cost. Its widespread usage also allows for quick reproduction of our optimization results. It is used in a black-box manner so that any other commercial or in-house airfoil analysis tools can be incorporated into our optimization framework if necessary. Our detailed airfoil evaluation setup is given in Appendix B.

#### 3.2 Optimization

When a set of solutions is given, the most optimal solution within the set can be determined without difficulty for single-objective optimization problems, which is the case for most of the previous airfoil optimization studies (Tang et al., 2020; Ashenafi et al., 2022; Chen & Ahmed 2020). However, for multi-objective optimization, multiple and potentially conflicting objectives must be considered simultaneously to determine the optimal answer in the solution set (Miettinen 2004; Gunantara 2018). If the designer has a quantitative ranking of the objectives, these objectives can be combined together to formulate a single-objective problem, but when no such ranking exists, constructing a Pareto-front is the most common methodology (Barron & Barrett 1996; Das & Dennis 1997; Chang 2008), which has applications in the design of architected materials (Ghachi et al., 2020; Vangelatos et al., 2021) and turbo-machinery (Schlieter & Długosz 2020; Xu et al., 2021; Chehouri et al., 2016; Rodrigues et al., 2016; Wang et al., 2011; Rao et al., 2007), process engineering (Nguyen 2021; Gao et al., 2018; Wang et al., 2020), shape design (Li et al., 2020; Correia et al., 2021; Ciardiello et al., 2020), and structural engineering (Fox et al., 2019; Afshari et al., 2019).

We pose the multi-objective optimization problem as

$$\mathbf{w}_{opt} = \underset{\mathbf{w} \in \mathcal{W}}{\operatorname{argmax}}(\mathbf{f}(\mathbf{w})), \quad (3)$$

where  $\mathbf{f}(\mathbf{w}) = [f_1(\mathbf{w}), f_2(\mathbf{w}), \dots, f_k(\mathbf{w})]$ . Here,  $f_1, \dots, f_k$  are the  $K$  objectives to be maximized, and  $\mathbf{w}$  is the design variable vector. Generally,  $\mathbf{w}$  is a  $d$ -dimensional vector defined over a bounded set  $\mathcal{W} \subset \mathbb{R}^d$  representing  $d$  continuous variables.  $\{\mathbf{w}_{opt}\}$  is a set of Pareto-optimal solution vectors, i.e., vectors that are not Pareto-dominated by any other vectors. For the reader's convenience, it is noted that a design variable vector  $\hat{\mathbf{w}}$  is Pareto-dominated by another design variable vector  $\tilde{\mathbf{w}}$  if  $f_k(\hat{\mathbf{w}}) \leq f_k(\tilde{\mathbf{w}})$  for all  $k \in \{1, \dots, K\}$ . To obtain the Pareto-front, especially when objectives cannot be weighted or when a non-convex black-box function is considered,



evolutionary or GAs are a natural choice (Wang et al., 2020; Gao et al., 2000). In fact, these algorithms have been commonly implemented in many previous aerodynamic optimization studies due to their gradient-free nature and wide search domain (Zhao et al., 2014; Skinner & Zare-Behtash 2018; Rahmad et al., 2020; Akram & Kim 2021). An alternate choice is the Bayesian optimization method, which has been proven to be efficient when the cost functions are expensive to compute (e.g., when using experiments or CFD as an evaluation tool; Sheikh & Marcus 2022).

Our study considers a bi-objective ( $K = 2$ ) 2D airfoil shape optimization. In particular, we optimize the shape of a subsonic airfoil operating in an incompressible flow with  $Re \equiv Uc/\nu$  of  $1 \times 10^6$ , where  $U$  and  $\nu$  are the free-stream flow speed and fluid kinematic viscosity, respectively, and  $c$  is the airfoil chord length. The parameter to be optimized is the morphing weight vector for the DbM technique, defined as:

$$\mathbf{w} \equiv (w_1, \dots, w_{25}) \in \mathcal{D}^{25}, \quad (4)$$

where  $\mathcal{D} = [-1, 1] \subset \mathbb{R}$  and  $w_i$  ( $i = 1, 2, \dots, 25$ ) is the weight applied to the  $i^{\text{th}}$  baseline shape. The design objectives are the maximum lift-drag ratio over all possible angles of attack  $\alpha$ , i.e.,  $f_1(\mathbf{w}) = CLD_{max}(\mathbf{w})$ , and the difference between the stall angle  $\alpha_s$  and the angle where the maximum lift-drag ratio occurs, i.e.,  $f_2(\mathbf{w}) = \Delta\alpha(\mathbf{w})$ , often called the stall angle tolerance. This particular combination of design objectives has applications in the design of vertical-axis wind turbines (Sheikh & Marcus 2019), and the precise definitions of these design objectives are explained in Appendix A. Both objectives are evaluated using XFOIL, which is efficient enough to be used with the GA.

We use a MATLAB-based variant of the popular NSGA-II algorithm `gamultiobj` (Deb et al., 2002), which is a controlled, elitist GA. Its practical employment can be found in Keane & Voutchkov (2020) for the purpose of airfoil design optimization, as in the case with ours. Our initial population consists of the single-objective optimums of each design target and random samples in the design space. A population size of 372 is used with a total of 3000 GA generations. Within each generation, solutions are actively ranked to maintain diversity and prevent overcrowding in the Pareto-optimal solution set. Our setup was tested using the commonly used set of ‘ZDT’ benchmark problems for multi-objective problems, as suggested by Zitzler et al., (2000). The test problems and validation results are detailed in Appendix C.

## 4. Results

A Pareto-front on the  $\Delta\alpha - CLD_{max}$  objective plane resulting from a total of 3000 generations of the GA runs is depicted in Fig. 11. See Appendix C for how we validated the maximum generation number. The convergence of the front is confirmed by the large number of generations with a population size of 372, involving around 1.1 million XFOIL evaluations of  $CLD_{max}$  and  $\Delta\alpha$ . Without duplicates, a set of 80 Pareto-optimal airfoil shapes was obtained via DbM from the 25 chosen baseline shapes. For comparison, the whole UIUC database (Selig, 2022), as well as the baseline cases, are evaluated and plotted in Fig. 11 together. It is noted that baseline #19 has zero  $CLD_{max}$  and  $\Delta\alpha$  because it is intentionally mirrored, and XFOIL failed to evaluate its aerodynamic performance. We assigned zero values to cases of failure like this because they represented airfoil geometries found to be aerodynamically unviable in the XFOIL space. The GA optimization successfully developed the Pareto-front, with two ends at  $(CLD_{max}, \Delta\alpha) = (30.63, 40^\circ)$  and  $(CLD_{max}, \Delta\alpha) = (264.17, 11^\circ)$ . Even in the largest maximum lift-

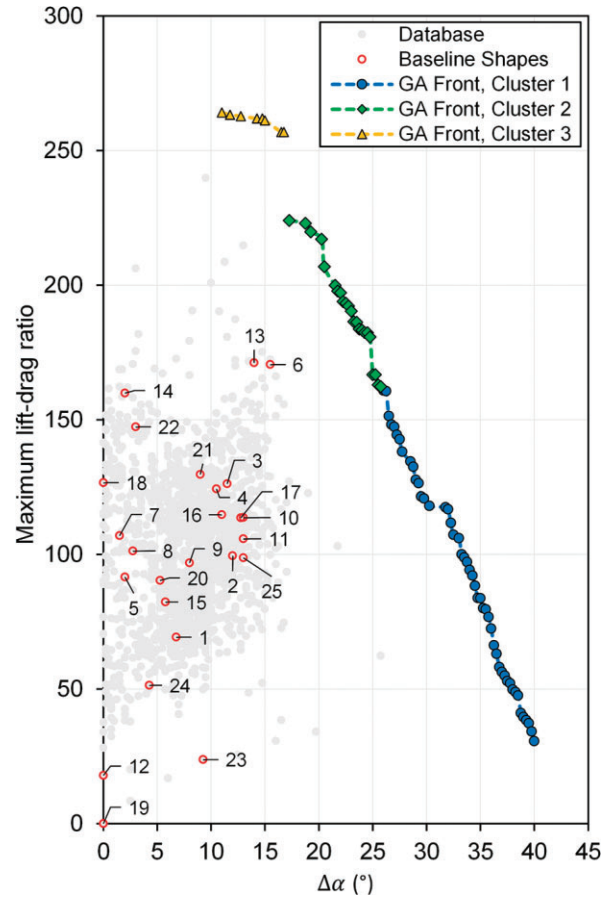


**Figure 11:** The Pareto-front consisting of the optimal airfoil shapes, resulting from the NSGA-II 3000 generation runs. The grey points are the whole evaluation outcomes of the UIUC reference database (Selig, 2022), with the DbM baseline cases in the present study highlighted as red hollow circles with respective indices. See Appendix D for the clustering.  $Re_{chord} = 1 \times 10^6$ .

drag ratio case, the angle of attack gap between the stall and design point is  $11^\circ$ , providing the airfoil with a decent tolerant range for off-design operations.

The Pareto-front is divided into three different clusters, each constituting a segment of the front that does not overlap with the others. It is worth noting that the non-overlapping division of the front is a result of clustering through Principal Component Analysis (PCA) rather than being manually assigned. The details of the clustering are provided in Appendix D.

Fig. 12 depicts nine representative optimal airfoil shapes on the Pareto-front, arranged in ascending order of  $CLD_{max}$ . From each cluster, three airfoil shapes with distinct objective function values have been selected for representation. Also, note that Fig. 12a shows the extreme case of the smallest  $CLD_{max}$  and largest  $\Delta\alpha$ , while Fig. 12i depicts the opposite extreme of the largest  $CLD_{max}$  and smallest  $\Delta\alpha$ . It can be seen that within each cluster, the overall shape remains unchanged, with only a gradual decrease in airfoil thickness as  $CLD_{max}$  increases. Since thin airfoils such as bird-like airfoils (Ananda & Selig, 2018), e.g., #13 and #14 of the baseline shapes, are known for their high  $CLD$  performance, the trend of airfoil thickness observed in the Pareto-front appears to be reasonable.

Cluster 1, made up of 48 optimal airfoil shapes, resembles the total mean of the Pareto-front, which is the average of all airfoil shapes on the Pareto-front (see Fig. 14a). This makes sense



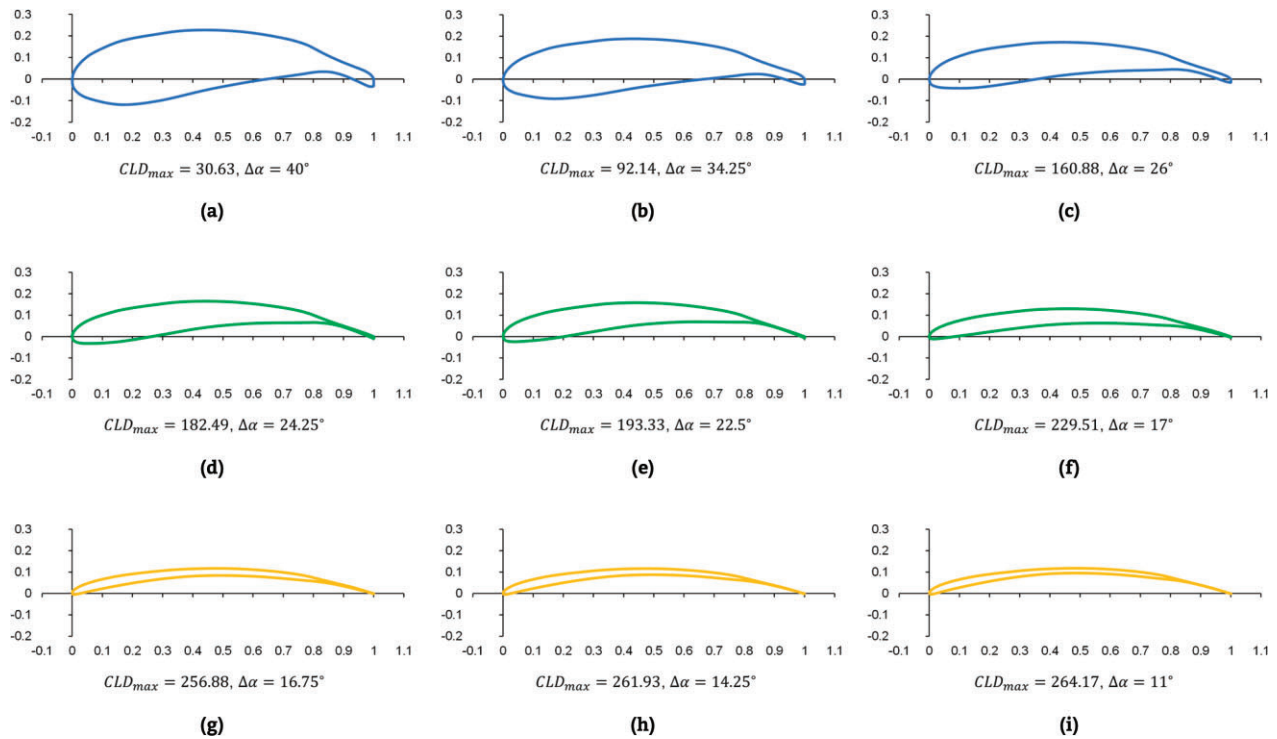


**Figure 12:** Nine representative Pareto-optimal airfoil shapes. (a)–(c) are in cluster 1, (d)–(f) are in cluster 2, and (g)–(i) are in cluster 3. See Appendix D for the clustering.

as they make up the majority of airfoil shapes located on the front. Moreover, this cluster is located near the origin in the PCA-projected weight space (see Fig. D1 in Appendix D), indicating that no radical morphing of the airfoil shape took place from the mean shape.

Next, cluster 2 contains 24 optimal airfoil shapes. Compared to those in cluster 1, the most distinguishing feature is their narrow trailing edge regions, which are typically favorable for increasing lift. However, these airfoils are not greatly different from the origin in the PCA-projected weight space and are close to the total mean Pareto-front.

Finally, eight optimal airfoil shapes are found in cluster 3 from the optimization. This cluster includes the airfoil shapes experiencing more drastic morphing than the other clusters. This is manifested by the fact that they are the thinnest airfoils where the leading edge region's thickness also becomes narrow.

The mean weight distributions with respect to 25 original baseline shapes are shown in Fig. 13. Overall, the weight distributions of the three clusters conform to the weight distribution of the total mean. It turned out that baseline shape #13 (model name: AS6097) was commonly the most significant for morphing. Since this baseline shape has the best in  $CLD_{max}$  and the second best in  $\Delta\alpha$  among the 25 baseline shapes (see Fig. 11), it was likely to persist in the GA runs over generations against the selection pressure that only sorts out dominant individuals in terms of both  $CLD_{max}$  and  $\Delta\alpha$ . However, excellence in the objectives of an individual baseline shape does not necessarily guarantee its survival, which is the case for the globally best baseline shape #6 (model name: AH 79-100C). An individual's superior 'phenotype' may be no longer revealed or even suppressed after the morphing is done and all 'genes' are mixed up. In the same sense, inferiority in the objectives of an individual does not necessarily result in elimination, as demonstrated by the 'mirrored' baseline #19.

As discussed from the examination of the morphed airfoil shapes, both cluster 1 and 2 show no significant differences from the total mean Pareto-front. Through small shape variations in shape from the total mean Pareto-front, as seen in Fig. 14a, reaching these optima would be relatively easy. In contrast, cluster 3 has a number of weights that are quite different from the mean (e.g., #6 and #11) and substantial morphing would be required if one starts with the total mean airfoil shape.

In the context of the present study, each axis obtained by PCA can be considered as a unique morphed airfoil shape because the 25 PCA coefficient vectors defined in the weight space  $\mathcal{D}^{25}$  are orthogonal to each other. These 25 new morphed airfoils span the entire design space and therefore can serve as alternative baseline shapes in lieu of the original ones. More importantly, the dominance of the first two PCA axes with respect to the data point variance, accounting for 95% of the total variance explained, suggests that the major geometric features of the 208 airfoil shapes we found through optimization are virtually generated by the morphing of these two new airfoils. A small variance of a PCA axis indicates that the data points are not significantly deviated from their mean on the axis. In other words, the baseline shape corresponding to this PCA axis has a marginal impact on morphing the airfoil shape for optimization.

Once we pick two baseline shapes from the first two dominant PCA axes, whose associated collocation vectors are denoted as, e.g.,  $\mathbf{P}_1$  and  $\mathbf{P}_2$ , and use them to morph the airfoil shape obtained from the total mean of the Pareto-optimal weight vector set, which corresponds to the mean collocation vector  $\mathbf{P}_{mean}$ , we gain a better understanding of how the morphing, especially along each PCA axis, influences major geometric changes in the optimal airfoil shapes. These airfoil shapes are depicted in Fig. 14, where the black and red surfaces are distinguished to emphasize that they represent the first and second halves of the collocation points, respectively. For example, we note that the orientation of

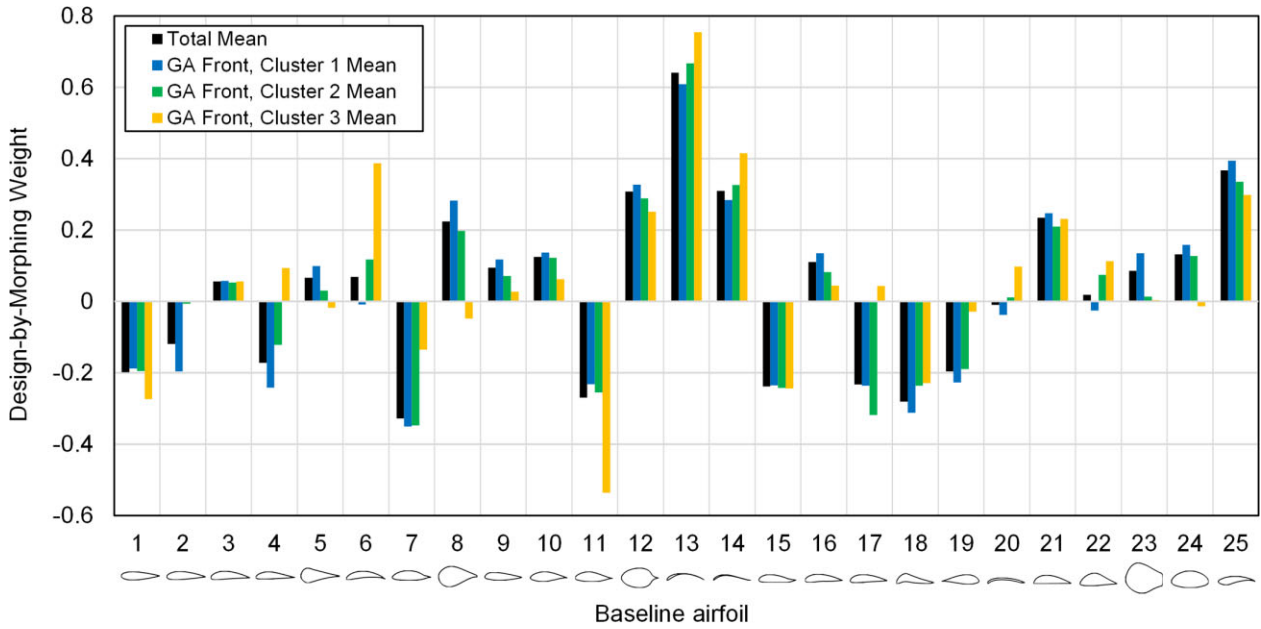


Figure 13: Mean weight distributions of the Pareto-optimal airfoil shapes with respect to 25 baseline airfoil shapes.

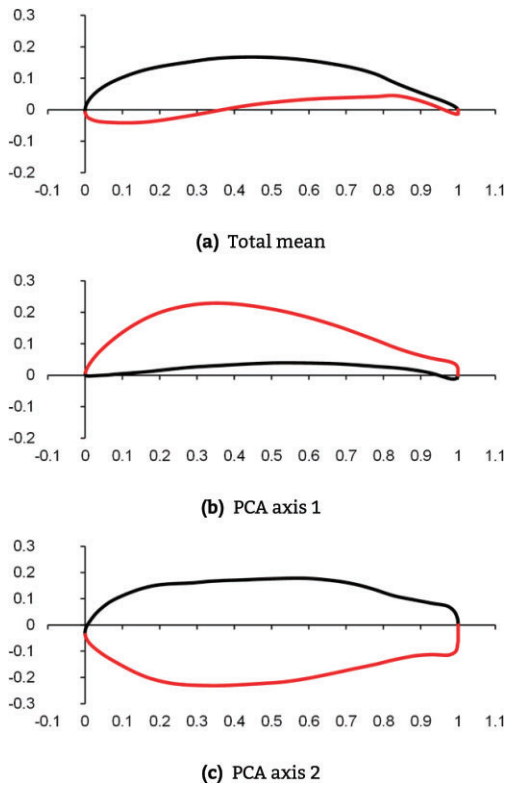


Figure 14: Morphed airfoil shapes generated by the optimal weight vectors, representing (a) the total mean of all optimal airfoils' weights, (b) the coefficients of the PCA axis having the most variance, and (c) the coefficients of the PCA axis having the second-most variance. The black and red surfaces correspond to the first and second half of the collocation points, respectively.

the two surfaces of  $P_1$  is mirrored in comparison to that of  $P_{mean}$ , meaning that the stronger the weight of PCA axis 1 in the positive direction is, the narrower the morphed airfoil shape gets.

### 5. Discussion

Most shape parametrization methods rely upon the careful selection of geometric constraints and parameters, which determines the likelihood of success. The fidelity offered by such methods largely depends on the number of parameters chosen. Moreover, these designs are limited by parametric constraints and implicit designer bias, making it difficult to perform extrapolation or make radical global changes. Data-driven methods typically rely on the assumption that the optimum solutions are not far from the training data set, which again limits the ability to make radical shape changes.

DbM, on the other hand, creates a design space that is not inhibited by geometric constraints, enables extrapolation from the design space, which is particularly useful for airfoil design, and is applicable to a wide range of engineering design problems. It does not suffer from the curse of dimensionality when parameterizing airfoils by control points and allows for a high-fidelity representation of airfoils without increasing the number of independent parameters in the problem. Using only 25 baseline shapes from the UIUC database, we were able to recreate 99.87% of the UIUC database with an MAE error <1%. We also showed that extraordinary and broad searches are possible using DbM. By applying it to the bi-objective shape optimization with the objectives of maximizing  $CLD_{max}$  and  $\Delta\alpha$ , we could achieve significant results compared to our baseline shapes. We posit that for the design parametrization of airfoils as well as other 2D/3D shapes, DbM should be the preferred method for creating an unconstrained, unbiased, and non-database-driven design space that allows for radical modifications, which can often result in non-conforming shapes. In this paper, our qualitative selection of 25 baseline shapes adequately spanned the design space with tolerable error. However, it would be possible that even a smaller number of baseline shapes than 25 could successfully construct the design space if some of the current baseline shapes were redundant. To further understand DbM, our future work will focus on performing sensitivity analysis of DbM on the baseline shape selection and applying DbM for the design of turbo-machinery.

## 6. Conclusions

The DbM design strategy creates a design space that contains novel and radical 2D airfoils that are not constrained by geometric parameters or designer bias. Optimization within the design space created, for the dual objectives of  $CLD_{max}$  and  $\Delta\alpha$ , resulted in remarkable improvements in both objectives and provided a Pareto-front of optimal airfoil designs. The final airfoils showed significant advancements compared to the input baseline shapes.

Overall, in our optimization study with respect to the 2D airfoil optimization problem, DbM is a suitable method for design space creation. In addition, our methodology is highly adaptable and can be utilized for shape optimization of other fluid machinery. Our ongoing work includes the applications of DbM in conjunction with Bayesian optimization to 3D airfoil optimization and vertical-axis wind turbine optimization problems.

## Acknowledgments

The authors would like to thank Prof. Ömer Savaş, affiliated with the University of California, Berkeley for providing insightful discussions regarding airfoils and aerodynamics. The authors acknowledge the use of the Extreme Science and Engineering Discovery Environment, supported by National Science Foundation grant number ACI-1548562 through allocation TG-CTS190047.

## Data and Materials Availability

The data needed to evaluate the conclusions are present in the paper and Appendices. The data files and optimization setup will be posted in a public repository upon publication of the paper.

## Funding

No funding information needs to be disclosed. No funding was received.

## Nomenclature

### Alphabets

- P:**  $y$ -coordinate collocation vector of a morphed airfoil  
**S:**  $y$ -coordinate collocation vector of a baseline airfoil  
**c:** Airfoil chord length (m)  
**d:** Drag force of an airfoil per unit span ( $N\ m^{-1}$ )  
**l:** Lift force of an airfoil per unit span ( $N\ m^{-1}$ )  
**U:** Free-stream flow speed ( $m\ s^{-1}$ )  
**w:** Design-by-Morphing weight factor

### Greek Letters

- $\alpha$ : Airfoil angle of attack ( $^\circ$ )  
 $\alpha_s$ : Airfoil stall angle ( $^\circ$ )  
 $\Delta\alpha$ : Stall angle tolerance, the range of  $\alpha$  between the stall point and the maximum lift-drag ratio point ( $^\circ$ )  
 $\nu$ : Fluid kinematic viscosity ( $m^2\ s^{-1}$ )  
 $\rho$ : Fluid density ( $kg\ m^{-3}$ )

## Dimensionless Groups

- Re: Reynolds number based on airfoil chord length,  $Uc/\nu$   
 $C_d$ : Drag coefficient of an airfoil per unit span,  $2d/(\rho U^2 c)$   
 $C_l$ : Lift coefficient of an airfoil per unit span,  $2l/(\rho U^2 c)$

- CLD: Lift-drag ratio of an airfoil,  $C_l/C_d$   
 $CLD_{max}$ : Maximum lift-drag ratio of an airfoil,  $\max_{\alpha} CLD(\alpha)$

## Conflict of interest statement

The authors declare no conflict of interest in this work.

## References

- Afshari, H., Hare, W., & Tesfamariam, S. (2019). Constrained multi-objective optimization algorithms: Review and comparison with application in reinforced concrete structures. *Applied Soft Computing*, **83**, 105631. <https://doi.org/10.1016/j.asoc.2019.105631>.
- Airfoil Tools (2022). Retrieved January 31, 2023, from <http://airfoiltools.com/>.
- Akram, M. T., & Kim, M.-H. (2021). CFD Analysis and Shape Optimization of Airfoils Using Class Shape Transformation and Genetic Algorithm—Part I. *Applied Sciences*, **11**(9), 3791. <https://doi.org/10.3390/app11093791>.
- Ali, Q. S., & Kim, M.-H. (2021). Design and performance analysis of an airborne wind turbine for high-altitude energy harvesting. *Energy*, **230**, 120829. <https://doi.org/10.1016/j.energy.2021.120829>.
- Ananda, G. K., & Selig, M. S. (2018). Design of bird-like airfoils. in 2018 AIAA Aerospace Sciences Meetingp. 0310, Kissimmee, Florida: AIAA Inc.,
- Ashenafi, Y., Pandita, P., & Ghosh, S. (2022). Reinforcement learning-based sequential batch-sampling for bayesian optimal experimental design. *Journal of Mechanical Design*, **144**(9), 091705. <https://doi.org/10.1115/1.4054631>.
- Barron, F. H., & Barrett, B. E. (1996). Decision quality using ranked attribute weights. *Management Science*, **42**(11), 1515–1523. <https://doi.org/10.1287/mnsc.42.11.1515>.
- Batten, W., Bahaj, A., Molland, A., & Chaplin, J. (2006). Hydrodynamics of marine current turbines. *Renewable Energy*, **31**(2), 249–256. <https://doi.org/10.1016/j.renene.2005.08.020>.
- Besnard, E., Schmitz, A., Boscher, E., Garcia, N., & Cebeci, T. (1998). Two-dimensional aircraft high lift system design and optimization. in 36th AIAA Aerospace Sciences Meeting and Exhibit Reno, NV, U.S.A: American Institute of Aeronautics and Astronautics.
- Buhmann, M. D. (2003). Radial basis functions: theory and implementations. *Cambridge Monographs on Applied and Computational Mathematics* Cambridge: Cambridge University Press. <https://doi.org/10.1017/CBO9780511543241>
- Chang, C.-T. (2008). Revised multi-choice goal programming. *Applied Mathematical Modelling*, **32**(12), 2587–2595. <https://doi.org/10.1016/j.apm.2007.09.008>.
- Chehouri, A., Younes, R., Ilinca, A., & Perron, J. (2015). Review of performance optimization techniques applied to wind turbines. *Applied Energy*, **142**, 361–388. <https://doi.org/10.1016/j.apenergy.2014.12.043>.
- Chehouri, A., Younes, R., Ilinca, A., & Perron, J. (2016). Wind turbine design: multi-objective optimization. in *Wind Turbines - Design, Control and Applications* Rijeka: InTech. <https://doi.org/10.5772/63481>
- Chen, W., & Ahmed, F. (2020). PaDGAN: Learning to generate high-quality novel designs. *Journal of Mechanical Design*, **143**(3), 031703. <https://doi.org/10.1115/1.4048626>.
- Chen, W., Fuge, M., & Chazan, J. (2017). Design manifolds capture the intrinsic complexity and dimension of design spaces. *Journal of Mechanical Design*, **139**(5), 051102. <https://doi.org/10.1115/1.4036134>.



- Chen, W., & Chiu, K., & Fuge, M. D. (2020). Airfoil design parametrization and optimization using bézier generative adversarial networks. *AIAA Journal*, **58**(11), 4723–4735. <https://doi.org/10.2514/1.J059317>.
- Ciardello, A., Rosso, F., Dell’Olmo, J., Ciancio, V., Ferrero, M., & Salata, F. (2020). Multi-objective approach to the optimization of shape and envelope in building energy design. *Applied Energy*, **280**, 115984. <https://doi.org/10.1016/j.apenergy.2020.115984>.
- Cinquegrana, D., & Iuliano, E. (2018). Investigation of adaptive design variables bounds in dimensionality reduction for aerodynamic shape optimization. *Computers & Fluids*, **174**, 89–109. <https://doi.org/10.1016/j.compfluid.2018.07.012>.
- Correia, V. F., Moita, J. S., Moleiro, F., & Soares, C. M. M. (2021). Optimization of metal–ceramic functionally graded plates using the simulated annealing algorithm. *Applied Sciences*, **11**(2), 729. <https://doi.org/10.3390/app11020729>.
- Das, I., & Dennis, J. E. (1997). A closer look at drawbacks of minimizing weighted sums of objectives for Pareto set generation in multicriteria optimization problems. *Structural Optimization*, **14**(1), 63–69. <https://doi.org/10.1007/BF01197559>.
- Deb, K., Pratap, A., Agarwal, S., & Meyarivan, T. (2002). A fast and elitist multiobjective genetic algorithm: NSGA-II. *IEEE Transactions on Evolutionary Computation*, **6**(2), 182–197. <https://doi.org/10.1109/4235.996017>.
- Drela, M. (1989). Xfoil: An analysis and design system for low reynolds number airfoils. *Lecture Notes in Engineering*, **54** 1–12. [https://doi.org/10.1007/978-3-642-84010-4\\_1](https://doi.org/10.1007/978-3-642-84010-4_1).
- Drela, M. (1998). Pros & Cons of Airfoil Optimization, pp. 363–381. [https://doi.org/10.1142/9789812815774\\_0019](https://doi.org/10.1142/9789812815774_0019)
- Elham, A., & van Tooren, M. J. (2014). Winglet multi-objective shape optimization. *Aerospace Science and Technology*, **37**, 93–109. <https://doi.org/10.1016/j.ast.2014.05.011>.
- Farin, G. (1993). The bernstein form of a bézier curve. in *Curves and Surfaces for Computer-Aided Geometric Design*, pp. 41–63, Cambridge, MA, USA: Elsevier.
- Fox, A. D., Corne, D. W., Mayorga Adame, C. G., Polton, J. A., Henry, L.-A., & Roberts, J. M. (2019). An efficient multi-objective optimization method for use in the design of marine protected area networks. *Frontiers in Marine Science*, **6**, 17. <https://doi.org/10.3389/fmars.2019.00017>.
- Gao, H., Zhang, Y., Zhou, X., & Li, D. (2018). Intelligent methods for the process parameter determination of plastic injection molding. *Frontiers of Mechanical Engineering*, **13**(1), 85–95. <https://doi.org/10.1007/s11465-018-0491-0>.
- Gao, Y., Shi, L., & Yao, P. (2000). Study on multi-objective genetic algorithm. in *Proceedings of the 3rd World Congress on Intelligent Control and Automation (Cat. No.00EX393)*, vol. **1**, pp. 646–650, Hefei, China: IEEE.
- Ghachi, R. F., Alnahhal, W. I., Abdeljaber, O., Renno, J., Tahidul Haque, A. B. M., Shim, J., & Aref, A. (2020). Optimization of viscoelastic metamaterials for vibration attenuation properties. *International Journal of Applied Mechanics*, **12**(10), 2050116. <https://doi.org/10.1142/S1758825120501161>.
- Ghoman, S., Wang, Z., Chen, P., & Kapania, R. (2012). A POD-based reduced order design scheme for shape optimization of air vehicles. 53rd AIAA/ASME/ASCE/AHS/ASC Structures, Structural Dynamics and Materials Conference Honolulu, Hawaii. <https://doi.org/10.2514/6.2012-1808>
- Giguère, P., & Selig, M. S. (1998). New airfoils for small horizontal axis wind turbines. *Journal of Solar Energy Engineering*, **120**(2), 108–114. <https://doi.org/10.1115/1.2888052>.
- Grasso, F. (2012). Hybrid optimization for wind turbine thick airfoils. in 53rd AIAA/ASME/ASCE/AHS/ASC Structures, Structural Dynamics and Materials Conference, Honolulu, Hawaii
- Gunantara, N. (2018). A review of multi-objective optimization: Methods and its applications. *Cogent Engineering*, **5**(1), 1502242. <https://doi.org/10.1080/23311916.2018.1502242>.
- Han, X., & Zingg, D. W. (2014). An adaptive geometry parametrization for aerodynamic shape optimization. *Optimization and Engineering*, **15**(1), 69–91. <https://doi.org/10.1007/s11081-013-9213-y>.
- He, X., Li, J., Mader, C. A., Yildirim, A., & Martins, J. R. (2019). Robust aerodynamic shape optimization—from a circle to an airfoil. *Aerospace Science and Technology*, **87**, 48–61. <https://doi.org/10.1016/j.ast.2019.01.051>.
- Hicks, R. M., & Henne, P. A. (1978). Wing design by numerical optimization. *Journal of Aircraft*, **15**(7), 407–412. <https://doi.org/10.2514/3.58379>.
- Jameson, A. (1988). Aerodynamic design via control theory. *Journal of Scientific Computing*, **3**(3), 233–260. <https://doi.org/10.1007/BF01061285>.
- Johnson, F. T., Tinoco, E. N., & Yu, N. J. (2005). Thirty years of development and application of cfd at boeing commercial airplanes, seattle. *Computers & Fluids*, **34**(10), 1115–1151. <https://doi.org/10.1016/j.compfluid.2004.06.005>.
- Jones, B. R., Crossley, W. A., & Lyrantzis, A. S. (2000). Aerodynamic and aeroacoustic optimization of rotorcraft airfoils via a parallel genetic algorithm. *Journal of Aircraft*, **37**(6), 1088–1096. <https://doi.org/10.2514/2.2717>.
- Ju, Y. P., & Zhang, C. H. (2012). Multi-point robust design optimization of wind turbine airfoil under geometric uncertainty. *Proceedings of the Institution of Mechanical Engineers, Part A: Journal of Power and Energy*, **226**(2), 245–261. <https://doi.org/10.1177/0957650911426540>.
- Keane, A. J., & Voutchkov, I. I. (2020). Robust design optimization using surrogate models. *Journal of Computational Design and Engineering*, **7**(1), 44–55. <https://doi.org/10.1093/jcde/qwaa005>.
- Kedward, L., Allen, C. B., & Rendall, T. (2020). Generic modal design variables for aerodynamic shape optimisation. in AIAA AVIATION 2020 FORUM, American Institute of Aeronautics and Astronautics.
- Kenway, G. K. W., & Martins, J. R. R. A. (2016). Multipoint aerodynamic shape optimization investigations of the common research model wing. *AIAA Journal*, **54**(1), 113–128. <https://doi.org/10.2514/1.j054154>.
- Koroglu, S. M., & Ozkol, I. (2019). optimization of an airfoil characteristics to minimize the turn radius of a small unmanned aerial vehicle. 2019 IEEE 10th International Conference on Mechanical and Aerospace Engineering (ICMAE). pp 67–73. <https://doi.org/10.1109/icmae.2019.8880954>.
- Kulfan, B., & Bussoletti, J. (2006). “Fundamental” parameteric geometry representations for aircraft component shapes. in Portsmouth, Virginia 11th AIAA/ISSMO Multidisciplinary Analysis and Optimization Conference, American Institute of Aeronautics and Astronautics.
- Lafountain, C., Cohen, K., & Abdallah, S. (2010). Use of xfoil in design of camber-controlled morphing uavs. *Computer Applications in Engineering Education*, **20**(4), 673–680. <https://doi.org/10.1002/cae.20437>.
- Lamouin, H., & Waggenspack, N. (1994). NURBS-based free-form deformations. *IEEE Computer Graphics and Applications*, **14**(6), 59–65. <https://doi.org/10.1109/38.329096>.
- Li, J.-Y., Li, R., Gao, Y., & Huang, J. (2010). Aerodynamic optimization of wind turbine airfoils using response surface techniques. *Proceedings of the Institution of Mechanical Engineers, Part A: Journal*

- of Power and Energy, **224**(6), 827–838. <https://doi.org/10.1243/09576509JPE888>.
- Li, X., Yang, K., Bai, J., & Xu, J. (2013). A method to evaluate the overall performance of the CAS-W1 airfoils for wind turbines. *Journal of Renewable and Sustainable Energy*, **5**(6), 063118. <https://doi.org/10.1063/1.4841056>.
- Li, Y., Wei, K., Yang, W., & Wang, Q. (2020). Improving wind turbine blade based on multi-objective particle swarm optimization. *Renewable Energy*, **161**, 525–542. <https://doi.org/10.1016/j.renene.2020.07.067>.
- Lumsdaine, E., Johnson, W. S., Fletcher, L. M., & Peach, J. E. (1974). Investigation of the Kline-Fogleman airfoil section for rotor blade applications.
- Masters, D. A., Taylor, N. J., Rendall, T., Allen, C. B., & Poole, D. J. (2015). Review of aerofoil parameterisation methods for aerodynamic shape optimisation. in *53rd AIAA Aerospace Sciences Meeting*, Kissimmee, Florida: American Institute of Aeronautics and Astronautics.
- Masters, D. A., Taylor, N. J., Rendall, T. C. S., Allen, C. B., & Poole, D. J. (2017). Geometric comparison of aerofoil shape parametrization methods. *AIAA Journal*, **55**(5), 1575–1589. <https://doi.org/10.2514/1.J054943>.
- McGhee, R. J., Walker, B. S., & Millard, B. F. (1988). NASA technical memorandum 4062 Experimental results for the epller 387 airfoil at low reynolds numbers in the langley low-turbulence pressure tunnel.
- Miettinen, K. (2004). *Nonlinear multiobjective optimization*, New York, NY: Springer Science+Business Media, LLC.
- Morgado, J., Vizinho, R., Silvestre, M., & Páscoa, J. (2016). Xfoil vs cfd performance predictions for high lift low reynolds number airfoils. *Aerospace Science and Technology*, **52**, 207–214. <https://doi.org/10.1016/j.ast.2016.02.031>.
- Mueller, T. J., & DeLaurier, J. D. (2003). Aerodynamics of small vehicles. *Annual Review of Fluid Mechanics*, **35**(1), 89–111. <https://doi.org/10.1146/annurev.fluid.35.101101.161102>.
- Nguyen, P. (2021). A review of Hybrid/combined methods for trajectory optimization of flight vehicles. *Journal of Physics: Conference Series*, **1958**(1), 012032. <https://doi.org/10.1088/1742-6596/1958/1/012032>.
- Oh, S., Jiang, C.-H., Jiang, C., & Marcus, P. S. (2018). Finding the optimal shape of the leading-and-trailing car of a high-speed train using design-by-morphing. *Computational Mechanics*, **62**(1), 23–45. <https://doi.org/10.1007/s00466-017-1482-4>.
- Piotrowski, M. G., & Zingg, D. W. (2022). Investigation of a smooth local correlation-based transition model in a discrete-adjoint aerodynamic shape optimization algorithm. *AIAA SCITECH 2022 Forum*. <https://doi.org/10.2514/6.2022-1865>.
- Poole, D. J., Allen, C. B., & Rendall, T. (2019). Efficient aerostuctural wing optimization using compact aerofoil decomposition. in *AIAA Scitech 2019 Forum*, San Diego, California: American Institute of Aeronautics and Astronautics.
- Rahmad, Y., Robani, M. D., Palar, P. S., & Zuhail, L. R. (2020). Single- and multi-objective optimization of a low-speed airfoil using genetic algorithm. 020005, Jakarta, Indonesia: Tangerang Selatan.
- Ramanujam, G., & Ozdemir, H. (2017). Improving airfoil lift prediction. *35th Wind Energy Symposium*. <https://doi.org/10.2514/6.2017-1999>.
- Rao, A. R., Scanlan, J. P., & Keane, A. J. (2007). Applying multiobjective cost and weight optimization to the initial design of turbine disks. *Journal of Mechanical Design*, **129**(12), 1303–1310. <https://doi.org/10.1115/1.2779899>.
- Ribeiro, A., Awruch, A., & Gomes, H. (2012). An airfoil optimization technique for wind turbines. *Applied Mathematical Modelling*, **36**(10), 4898–4907. <https://doi.org/10.1016/j.apm.2011.12.026>.
- Rodrigues, S., Bauer, P., & Bosman, P. A. (2016). Multi-objective optimization of wind farm layouts – Complexity, constraint handling and scalability. *Renewable and Sustainable Energy Reviews*, **65**, 587–609. <https://doi.org/10.1016/j.rser.2016.07.021>.
- Rogalsky, T., & Derksen, R. W. (2009). Bézier–parsec parametrization for airfoil optimization. *Canadian Aeronautics and Space Journal*, **55**(3), 163–174. <https://doi.org/10.5589/q10-002>.
- Ronsten, G. (1992). Static pressure measurements on a rotating and a non-rotating 2.375 m wind turbine blade. comparison with 2d calculations. *Journal of Wind Engineering and Industrial Aerodynamics*, **39**(1–3), 105–118. [https://doi.org/10.1016/0167-6105\(92\)90537-k](https://doi.org/10.1016/0167-6105(92)90537-k).
- Samareh, J. A. (2001). Survey of Shape Parameterization Techniques for High-Fidelity Multidisciplinary Shape Optimization. *AIAA Journal*, **39**(5), 877–884. <https://doi.org/10.2514/2.1391>.
- Sanaye, S., & Hassanzadeh, A. (2014). Multi-objective optimization of airfoil shape for efficiency improvement and noise reduction in small wind turbines. *Journal of Renewable and Sustainable Energy*, **6**(5), 053105. <https://doi.org/10.1063/1.4895528>.
- Schlieter, T., & Długosz, A. (2020). Structural optimization of aerofoils for many criteria, p 448–451. <https://doi.org/10.21495/5896-3-448>
- Schramm, U., Pilkey, W. D., DeVries, R. I., & Zebrowski, M. P. (1995). Shape design for thin-walled beam cross sections using rational B splines. *AIAA Journal*, **33**(11), 2205–2211. <https://doi.org/10.2514/3.12870>.
- Sederberg, T. W., & Parry, S. R. (1986). Free-form deformation of solid geometric models. *ACM SIGGRAPH Computer Graphics*, **20**(4), 151–160. <https://doi.org/10.1145/15886.15903>.
- Selig, M. S. (2022). UIUC airfoil database.
- Selig, M. S., Guglielmo, J. J., Broeren, A. P., & Giguère, P. (1995). *Summary of Low Speed Airfoil Data*, vol. 1, SoarTech Publications.
- Serani, A., & Diez, M. (2023). Parametric model embedding. *Computer Methods in Applied Mechanics and Engineering*, **404**, 115776. <https://doi.org/10.1016/j.cma.2022.115776>.
- Sheikh, H. M., & Marcus, P. S. (2019). Vertical axis wind turbine design using design-by-morphing and bayesian optimization. *APS Division of Fluid Dynamics Meeting Abstracts*, Q14–007.
- Sheikh, H. M., & Marcus, P. S. (2022). Bayesian optimization for mixed-variable, multi-objective problems. *Struct Multidisc Optim*, **65**(331).
- Sheikh, H. M., Shabbir, Z., Ahmed, H., Waseem, M. H., & Sheikh, M. Z. (2017). Computational fluid dynamics analysis of a modified Savonius rotor and optimization using response surface methodology. *Wind Engineering*, **41**(5), 285–296. <https://doi.org/10.1177/0309524X17709732>.
- Sheikh, H. M., Callan, T., Hennessy, K., & Marcus, P. (2021). Shape optimization methodology for fluid flows using mixed variable bayesian optimization and design-by-morphing. *APS Division of Fluid Dynamics Meeting Abstracts*, A15–004.
- Sheikh, H. M., Callan, T. A., Hennessy, K. J., & Marcus, P. S. (2022). Optimization of the Shape of a Hydrokinetic Turbine’s Draft Tube and Hub Assembly Using Design-by-Morphing with Bayesian Optimization. *Computer Methods in Applied Mechanics and Engineering*, **401**, 115654. <https://doi.org/10.1016/j.cma.2022.115654>.
- Skinner, S., & Zare-Behtash, H. (2018). State-of-the-art in aerodynamic shape optimisation methods. *Applied Soft Computing*, **62**, 933–962. <https://doi.org/10.1016/j.asoc.2017.09.030>.

- Sobester, A., & Barrett, T. (2008). Quest for a truly parsimonious airfoil parametrization scheme. *The 26th Congress of ICAS and 8th AIAA ATIO*, <https://doi.org/10.2514/6.2008-8879>.
- Sobieczky, H. (1999). Parametric airfoils and wings. in *Recent Development of Aerodynamic Design Methodologies*, vol. 65, pp. 71–87. Vieweg+Teubner Verlag.
- Sripawadkul, V., & Padulo, M., & Guenov, M. (2010). A comparison of airfoil shape parametrization techniques for early design optimization. in *13th AIAA/ISSMO Multidisciplinary Analysis Optimization Conference*, Fort Worth, Texas: American Institute of Aeronautics and Astronautics.
- Tang, Y., Long, T., Shi, R., Wu, Y., & Wang, G. G. (2020) Sequential radial basis function-based optimization method using virtual sample generation. *Journal of Mechanical Design*, 142(11), 111701. <https://doi.org/10.1115/1.4046650>.
- Toal, D. J. J., Bressloff, N. W., Keane, A. J., & Holden, C. M. E. (2010). Geometric filtration using proper orthogonal decomposition for aerodynamic design optimization. *AIAA Journal*, 48(5), 916–928. <https://doi.org/10.2514/1.41420>.
- Vangelatos, Z., Sheikh, H. M., Marcus, P. S., Grigoropoulos, C. P., Lopez, V. Z., Flamourakis, G., & Farsari, M. (2021). Strength through defects: A novel Bayesian approach for the optimization of architected materials. *Science Advances*, 7(41), eabk2218. <https://doi.org/10.1126/sciadv.abk2218>.
- Vicini, A., & Quagliarella, D. (1999). Airfoil and wing design through hybrid optimization strategies. *AIAA Journal*, 37(5), 634–641. <https://doi.org/10.2514/2.764>.
- Viswanath, A., Forrester, A. I. J., & Keane, A. J. (2011). Dimension Reduction for aerodynamic design optimization. *AIAA Journal*, 49(6), 1256–1266. <https://doi.org/10.2514/1.J050717>.
- Viswanath, A., Forrester, A. I. J., & Keane, A. J. (2014). Constrained Design Optimization Using Generative Topographic Mapping. *AIAA Journal*, 52(5), 1010–1023. <https://doi.org/10.2514/1.J052414>.
- Wang, D., Geng, L., Zhao, Y.-J., Yang, Y., Huang, Y., Zhang, Y., & Shen, H.-B. (2020). Artificial intelligence-based multi-objective optimization protocol for protein structure refinement. *Bioinformatics*, 36(2), 437–448. <https://doi.org/10.1093/bioinformatics/btz544>.
- Wang, X., Hirsch, C., Kang, S., & Lacor, C. (2011). Multi-objective optimization of turbomachinery using improved NSGA-II and approximation model. *Computer Methods in Applied Mechanics and Engineering*, 200(9–12), 883–895. <https://doi.org/10.1016/j.cma.2010.11.014>.
- Wendland, H. (2005). *Scattered Data Approximation*, 17, Cambridge monographs on applied and computational mathematics, Cambridge University Press.
- Xu, B., Li, Z., Zhu, Z., Cai, X., Wang, T., & Zhao, Z. (2021). The parametric modeling and two-objective optimal design of a downwind blade. *Frontiers in Energy Research*, 9, 708230. <https://doi.org/10.3389/fenrg.2021.708230>.
- Yonekura, K., & Watanabe, O. (2014). A shape parametrization method using principal component analysis in applications to parametric shape optimization. *Journal of Mechanical Design*, 136(12), 121401. <https://doi.org/10.1115/1.4028273>.
- Zhao, K., Gao, Z.-H., & Huang, J.-T. (2014). Robust design of natural laminar flow supercritical airfoil by multi-objective evolution method. *Applied Mathematics and Mechanics*, 35(2), 191–202. <https://doi.org/10.1007/s10483-014-1783-6>.
- Zitzler, E., Deb, K., & Thiele, L. (2000). Comparison of multiobjective evolutionary algorithms: Empirical results. *Evolutionary Computation*, 8(2), 173–195. <https://doi.org/10.1162/106365600568202>.

## Appendix A. Aerodynamic Optimization Objectives

Airfoil optimization has become a common practice in aerodynamic design problems that involve maximization of one or more performance parameters of airfoils. We mainly consider the following two performance parameters: the lift-drag ratio and stall angle. Given the flow speed  $U$ , fluid density  $\rho$ , and airfoil chord length  $c$ , the lift and drag coefficients of an airfoil per unit span at an angle of attack  $\alpha$ ,  $C_l$ , and  $C_d$ , are expressed as:

$$C_l(\alpha) \equiv \frac{l(\alpha)}{\frac{1}{2}\rho U^2 c}, \quad C_d(\alpha) \equiv \frac{d(\alpha)}{\frac{1}{2}\rho U^2 c}. \quad (\text{A1})$$

where  $l$  and  $d$  are lift and drag force per unit span, respectively, both of which change with respect to  $\alpha$ . In this paper, these parameters are predicted using XFOIL (Drela, 1989), a program for analyzing a subsonic 2D airfoil, with varying  $\alpha$  and then used for optimization. Based on  $C_l$  and  $C_d$ , the lift-drag ratio  $CLD$  is calculated as:

$$CLD(\alpha) = \frac{C_l(\alpha)}{C_d(\alpha)}. \quad (\text{A2})$$

On the other hand, we define the stall angle  $\alpha_s$  as an angle of attack where  $C_l$  reaches its first local maximum as the angle increases from  $0^\circ$ , or:

$$\alpha_s \equiv \min_{\alpha \geq 0} \alpha \text{ where } \exists \delta > 0 \text{ such that}$$

$$C_l(\alpha) \geq C_l(x) \quad \forall x \in [\alpha - \delta, \alpha + \delta]. \quad (\text{A3})$$

Note that this definition is more conservative than the typical definition of stalling, where the flow at the rear region begins to fully separate and  $C_l$  is globally maximized.  $\alpha_s$  is occasionally smaller than the global maximum of  $C_l$ . Nonetheless, this approach helps avoid overestimation of the stall angle, which is expected to occur in XFOIL due to the nature of its flow solver having a limited accuracy in stall and post-stall conditions.

$CLD$  and  $\alpha_s$  have been typically considered to be significant in characterizing airfoil performance. For example, when it comes to lift-type wind turbines, the point where  $CLD$  is maximized is often chosen as the design point. However, since wind turbines cannot always operate under design conditions,  $\alpha_s$  needs to be additionally considered to evaluate how far they run under increasing lift conditions. For well-designed airfoils,  $\alpha_s$  generally occurs later than the design point, which yields operational tolerance beyond the design point. Consequently, the stall angle tolerance  $\Delta\alpha$ , i.e., the range between these two angles of attack, expressed as

$$\Delta\alpha \equiv \max\left(0, \alpha_s - \underset{\alpha \in \mathbb{R}}{\operatorname{argmax}} CLD(\alpha)\right), \quad (\text{A4})$$

can be a proper choice to evaluate the off-design performance (Li et al., 2013). Fig. A1 depicts a schematic diagram of how  $CLD$  and  $\Delta\alpha$  are determined on airfoil performance curves.

## Appendix B. Baseline Airfoil Shapes and Evaluation

Our optimization methodology does not rely on one specific airfoil evaluation tool. To compare our results with previous literature and help future researchers quickly reproduce our results, we used XFOIL (Drela, 1989) in the present study. The two design objectives,  $CLD_{max}$  and  $\Delta\alpha$ , are obtained from the  $C_l$  and  $C_d$  data calculated by the XFOIL at different angles of attack (see Fig. A1).



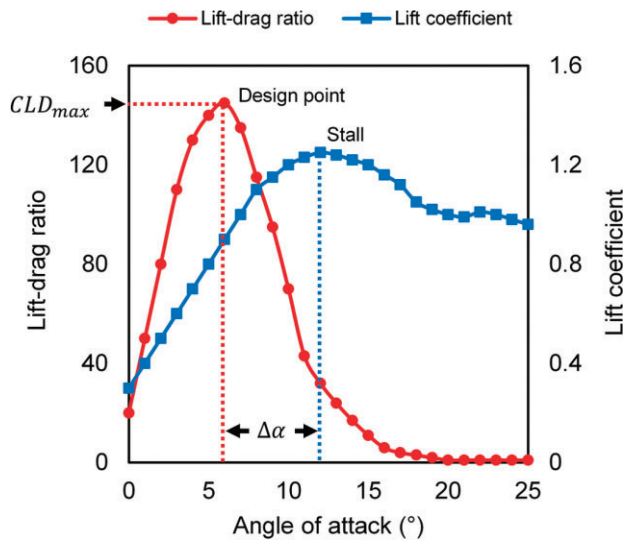


**Figure A1:** Schematic diagram of airfoil performance curves.

For improved efficiency and consistency, we used XFOIL to generate performance data and did not rely on any of its built-in paneling features. The conditioning and re-paneling of the morphed airfoil coordinates are custom-built at the end of our DbM algorithm, transforming the coordinates into 200 or 250 vortex panels with a relatively higher concentration where the curvature is high. To reduce evaluation time, we first performed a rough scan with an  $\alpha$  increment of  $1^\circ$  to estimate the range determining  $\Delta\alpha$ , and then finer scans for  $CLD_{max}$  and  $\Delta\alpha$  separately with an  $\alpha$  increment of  $0.25^\circ$  within and around the estimated range of  $\Delta\alpha$  from the initial rough scan.

It is worth noting that XFOIL uses a global Newton's method (Drela, 1989) to solve the boundary layer and transition equations simultaneously and uses the solution from the previous angle of attack as a starting guess. As a result, ill-conditioned airfoil coordinates and the occurrence of flow separation can both lead to non-convergence of the XFOIL evaluation. To ensure the robustness and correctness of our airfoil evaluation, our XFOIL wrapper attempts to reach convergence by restarting the root-finding with a fresh starting guess and gradually increasing the number of panels. If both attempts fail, the wrapper will check convergence at neighboring points, which will indicate whether flow separation occurs or not. Besides non-convergence, we further verify the correctness of Newton's method by comparing the calculated viscous and inviscid drag coefficients. The latter is determined purely by the potential flow theorem and has to be smaller than its viscous counterpart due to its neglect of the friction (viscous effect). Any angles with incorrect results will undergo the same treatment as non-converging ones, hence ensuring the correctness of our airfoil performance evaluation. A comparison between our XFOIL eval-

uation and an existing database of the same airfoils under the same flow conditions is provided in Table B1.

## Appendix C. Optimization Test Functions and Validation

We used the multi-objective problems suggested by Zitzler *et al.*, (2000) to test our GA setup. The details of the test functions are given in Table C1. All the test functions are aimed to be minimized with 25 variables in the given design space.

MATLAB's NSGA-II GA, a fast sorting and elitist multi-objective GA, was used for practical implementation. Initialization was performed through single-objective optimization for each objective and random sampling. A population size of 372 was used, with a total of 3000 maximum generations. The 'phenotype' crowding distance metric was used. This setup was validated on the test functions described above. All the problems were benchmarked with 25 variables ( $d = 25$ ) and two objective functions ( $K = 2$ ), as with the present airfoil optimization problem. The results of our setup on these four benchmark problems are shown in Fig. C1. The algorithm could accurately capture ZDT1, ZDT2, and ZDT4 and predict ZDT6, which is the most complicated due to its non-convex and non-uniform properties, reasonably well.


























## Appendix D. Airfoil Shape Clustering

To analyze the characteristics of the optimized airfoil shapes in detail, the airfoil shapes on the Pareto-front were classified into three clusters using  $k$ -means clustering based on the Euclidean distance with  $k = 3$ . The clustering was performed in the design variable space, or weight space, of  $\mathcal{D}^{25}$  rather than in the objective plane because the purpose of clustering was to identify common geometric features over different airfoil shapes as a result of the optimization. The selection of the cluster size was based on the PCA of the optimal weight vector set.

It should be noted here that the baseline shapes chosen might be linearly dependent. The distances in the PCA weight space, thus might not be rigorous as a morphed shape on the Pareto-front may be represented by another set of weights. However, this PCA analysis was used only to identify if qualitative classes within the Pareto-front could be found and clustered together and to glean some additional insights from our Pareto-front results.

Fig. D1 shows the projection of the 25D weight vector set to the 2D subspace spanned by the 2 PCA axes having the first- and second-most variance. The explained variance ratios of PCA axes 1 and 2 are 80.7% and 14.0%, respectively. On the other hand, the PCA axis of the third-most variance only accounts for 1.7% of the variance, affirming that the 2D projection in Fig. D1 adequately scatters the clusters. Based on this observation,  $k = 3$  was chosen to be the most appropriate cluster size.

**Table B1:** The model names, features, shape outlines, and XFOIL evaluation results of the 25 baseline shapes used by DbM in this paper. The coordinates of the baseline shapes are obtained from the UIUC airfoil coordinates database (Selig 2022). The airfoil evaluation results are obtained for an incompressible flow with a chord Reynold number of  $1 \times 10^6$ . The reference evaluation results are interpolated from the online XFOIL database (air, 2022); N/A indicates that no data are available.

Index	Model name	Series (Features)	Airfoil shape	Reference		Present	
				CLD <sub>max</sub>	Δα	CLD <sub>max</sub>	Δα
1	NACA 0012	NACA (4-digit)		75.6	8.50	69.3	6.75
2	NACA 2412	NACA (4-digit)		101.4	12.00	99.5	12.00
3	NACA 4412	NACA (4-digit)		129.4	1.75	126.2	11.50
4	E 205	Eppler		128.3	8.50	124.4	10.50
5	AH 81-K-144 W-F Klappe	Althaus		89.7	2.00	91.6	2.00
6	AH 79-100 C	Althaus		183.0	14.75	170.6	15.50
7	AH 79-K-143/18	Althaus		110.9	1.50	107.0	1.50
8	AH 94-W-301	Althaus		103.0	4.00	101.4	2.75
9	NACA 23112	NACA (5-digit)		98.6	6.75	96.9	8.00
10	NACA 64(2)-415	NACA (6-digit)		120.6	12.50	113.8	13.00
11	NACA 747(A)-315	NACA (7-digit)		111.5	12.00	105.8	13.00
12	Griffith 30% Suction	Griffith (Suction)		17.3	0.00	17.9	0.00
13	AS 6097	Selig (Bird-like)		N/A	N/A	171.2	14.00
14	E 379	Eppler (Bird-like)		N/A	N/A	160.0	2.00
15	Clark YS	Clark		85.7	5.25	82.3	5.75
16	Clark W	Clark		116.1	11.00	114.8	11.00
17	Clark Y	Clark		114.8	11.75	113.7	12.75
18	Chen	Chen		125.4	0.00	126.7	0.00
19	S2027 Mirrored	Selig (Mirrored)		N/A	N/A	0.00	0.00
20	GOE 417A	Gottingen (Thin plate)		86.7	5.25	90.4	5.25
21	GOE 611	Gottingen (Flat bottom)		125.6	9.00	129.7	9.00
22	Dragonfly Canard	Dragonfly		144.6	2.50	147.5	3.00
23	FX 79-W-470A	Wortmann (Fat)		N/A	N/A	23.9	9.25
24	Sikorsky DBLN-526	Sikorsky (Fat)		53.3	4.75	51.5	4.25
25	FX 82-512	Wortmann		99.1	14.75	98.7	13.00

**Table C1:** Benchmark test functions. All of the test functions are bi-objective with extended to  $n$ -dimensional constrained search space.

Problem	Bounds	Objective functions	Optima	Note
ZDT1	$w_i \in [0, 1]$ , $i = 1, \dots, n$	$f_1(\mathbf{w}) = w_1$ $f_2(\mathbf{w}) = g(\mathbf{w}) [1 - (f_1(\mathbf{w})/g(\mathbf{w}))^{1/2}]$ $g(\mathbf{w}) = 1 + 9 (\sum_{i=2}^n w_i) / (n - 1)$	$w_1 \in [0, 1]$ $w_i = 0,$ $i = 2, \dots, n$	convex
ZDT2	$w_i \in [0, 1]$ , $i = 1, \dots, n$	$f_1(\mathbf{w}) = w_1$ $f_2(\mathbf{w}) = g(\mathbf{w}) [1 - (f_1(\mathbf{w})/g(\mathbf{w}))^2]$ $g(\mathbf{w}) = 1 + 9 (\sum_{i=2}^n w_i) / (n - 1)$	$w_1 \in [0, 1]$ $w_i = 0,$ $i = 2, \dots, n$	non-convex
ZDT4	$w_1 \in [0, 1]$ $w_i \in [-5, 5]$ , $i = 2, \dots, n$	$f_1(\mathbf{w}) = w_1$ $f_2(\mathbf{w}) = g(\mathbf{w}) [1 - (f_1(\mathbf{w})/g(\mathbf{w}))^{1/2}]$ $g(\mathbf{w}) = 10n + \sum_{i=2}^n (w_i^2 - 10 \cos(4\pi w_i)) - 9$	$w_1 \in [0, 1]$ $w_i = 0,$ $i = 2, \dots, n$	non-convex
ZDT6	$w_i \in [0, 1]$ , $i = 1, \dots, n$	$f_1(\mathbf{w}) = 1 - \exp(-4w_1) \sin^6(6\pi w_1)$ $f_2(\mathbf{w}) = g(\mathbf{w}) [1 - (f_1(\mathbf{w})/g(\mathbf{w}))^2]$ $g(\mathbf{w}) = 1 + 9 [(\sum_{i=2}^n w_i) / (n - 1)]^{1/4}$	$w_1 \in [0, 1]$ $w_i = 0,$ $i = 2, \dots, n$	non-convex, non-uniform

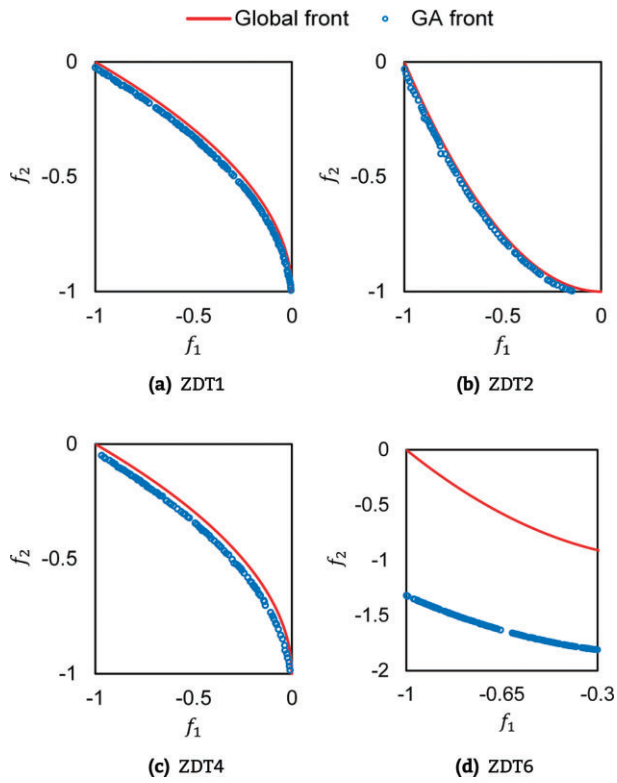


**Figure C1:** Multi-objective optimization of benchmark test functions using GA.

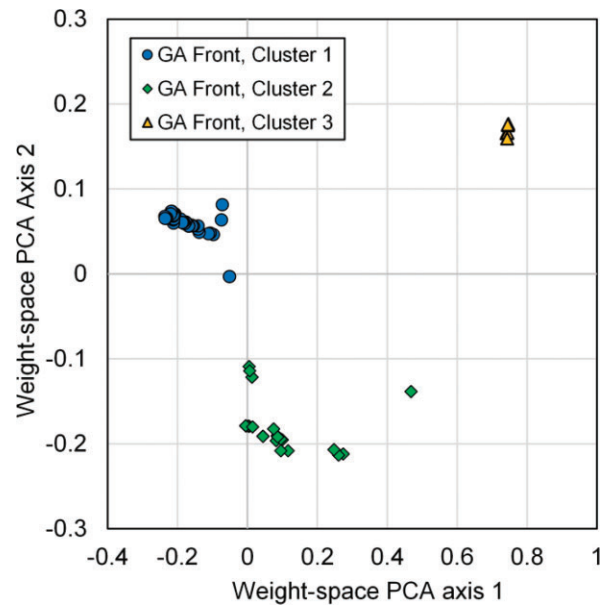


**Figure D1:** Projection of the 25D optimal weight vectors to the 2D subspace spanned by 2 PCA axes of the dominant variance. *k*-means clustering with a cluster size of 3 is used to identify the clusters.